NOVA SCHOOL OF SCIENCE & TECHNOLOGY

DEPARTMENT OF PHYSICS

CATARINA MELO DE JESUS MARQUES

Bachelor Degree in Science of Physics Engineering

OPTIMIZATION OF SPECTROSCOPIC TESTS OF FUNDAMENTAL PHYSICS:

FROM ESPRESSO TO THE ELT

PHYSICS ENGINEERING

NOVA University Lisbon
March, 2022

NOVA SCHOOL OF SCIENCE & TECHNOLOGY

DEPARTMENT OF PHYSICS

OPTIMIZATION OF SPECTROSCOPIC TESTS OF FUNDAMENTAL PHYSICS:

FROM ESPRESSO TO THE ELT

CATARINA MELO DE JESUS MARQUES

Bachelor Degree in Science of Physics Engineering

Adviser: Carlos J. A. P. Martins
Researcher, Centro de Astrofísica da Universidade do Porto

Contact Person: Maria Isabel S. Catarino
Assistant Professor, NOVA University Lisbon

Examination Committee:

Chair: André J. M. L. V. Wemans
Assistant Professor, NOVA University Lisbon

Rapporteur: Mauro A. M. Guerra
Assistant Professor, NOVA University Lisbon

Adviser: Carlos J. A. P. Martins
Researcher, Centro de Astrofísica da Universidade do Porto

PHYSICS ENGINEERING

NOVA University Lisbon
March, 2022

Optimization of Spectroscopic Tests of Fundamental Physics:
from ESPRESSO to the ELT

Acknowledgements

This research was made possible with the help of several people, to whom I express my gratitude.

To my supervisor, Researcher Carlos Martins, for giving me the opportunity to carry out this research. For his help, motivation, and availability during the realization of this work. His demand and humility allied to his knowledge were crucial points for my learning, integration in the area, commitment and preparation of my future.

To Professor Isabel Catarino for her advice, motivation and help throughout all the years at NOVA School of Science and Technology.

To all my CosmoESPRESSO colleagues for the worthwhile discussions, mutual help and companionship that made my experience during the dissertation excellent.

To my friends from the Physics Engineering course that made my time at NOVA School of Science and Technology unforgettable.

Last, but clearly not the least, to my family, for everything they represent to me. For their total support, for the help in finding solutions and overcoming difficulties, and without whom I would not be where I am today.

Abstract

Extremely large telescopes allow us a huge advance in knowledge in the field of Astrophysics, leading not only to better images of our cosmos but also to a deeper expertise of it.

Noted as "the world's biggest eye on the sky", the European Southern Observatory (ESO) Extremely Large Telescope (ELT) is under construction in the Chile's Atacama Desert. This optical/near-infrared telescope is designed to cover a wide range of scientific possibilities. In particular, the study of the dark universe and fundamental physics using one of its instruments, the ArmazoNes high Dispersion Echelle Spectrograph (ANDES).

Bearing in mind that instruments are designed with specific scientific goals, but subject to various technical and financial limitations, an instrument of this caliber requires a high level of planning both in its design and construction. This work focuses on the development of computational tools that can optimize the scientific return of fundamental physics astrophysical tests (including measurements of redshift drift and fine-structure constant) using ANDES and for its various possible configurations. In detail, it focuses on quantifying the scientific impact of possible configurations and the consequent identification of key parameters for the respective scientific trade-offs.

This is an important outcome for the ANDES Phase B studies, and it will ultimately lead to the definition of an optimized observational strategy, which in turn will be the starting point for the subsequent planning of the scientific exploitation of the telescope and instrument.

Keywords: ANDES, redshift drift, fine-structure constant

Resumo

Os telescópios extremamente grandes permitem-nos um enorme avanço do conhecimento na área da Astrofísica, levando não só a melhores imagens do nosso cosmos como também a um aprofundar do conhecimento do mesmo.

Apontado como "o maior olho do mundo virado para o céu", o Extremely Large Telescope (ELT) do Observatório Europeu do Sul (ESO) encontra-se em construção no deserto do Atacama, Chile. Este telescópio ótico/infravermelho, equipado com tecnologia de ponta, foi desenhado para cobrir uma ampla gama de possibilidades científicas. Em particular, o estudo do universo escuro e da física fundamental com recurso a um dos seus instrumentos, o ArmazoNes high Dispersion Echelle Spectrograph (ANDES).

Tendo em conta que os instrumentos são projetados com objetivos científicos específicos, mas sujeitos a várias limitações técnicas e financeiras, um instrumento deste calibre requer um grande nível de planeamento tanto no seu desenho como construção. Este trabalho foca-se no desenvolvimento de ferramentas computacionais que possam otimizar o retorno científico de testes astrofísicos de física fundamental (incluindo medições do *redshift drift* e do valor da constante de estrutura fina) utilizando o ANDES e para as várias configurações possíveis deste. Em pormenor, foca-se na quantificação do impacto científico de possíveis configurações e consequente identificação dos parâmetros-chave para as respetivas compensações científicas.

Este é um resultado importante para os estudos da Fase B do ANDES e, em última análise, levará à definição de uma estratégia de observação otimizada, que por sua vez, será o ponto de partida para o planeamento posterior da exploração científica do telescópio e instrumento.

Palavras-chave: ANDES, *redshift drift*, constante de estrutura fina

Contents

List of Figures

List of Tables

Glossary

Active Galactic Nuclei Very bright nucleus of a galaxy, in particular when its central region is much more luminous than the rest of the galaxy. At the center of an active galaxy is a supermassive black hole that accumulates all the material for the central region of the galaxy, becoming an extremely dense region. The accretion in a supermassive black hole is the source of the extreme luminosity of an Active Galactic Nuclei (AGN). 5

Dichroic Filter Filter made of highly polished glass and coated with multiple layers of thin dielectric films. This filter will, at a given angle of incidence, reflect undesired wavelengths and transmit the remaining ones. 16, 18

Free Spectral Range The largest wavelength band in a given order that does not overlap with the identical band in an adjacent order. 13, 14

Grating Optical element composed of a large number of thin, equidistant, parallel lines. A grating is said to be a transmission or reflection grating according to how the light behaves when passing through the lines, transmission if it passes between the lines, reflection if the incident light between the lines is reflected. It can also be a diffraction grating if it scatters the incident light into its components by wavelength. 13

Light Cone Double-cone centralized at each event in spacetime. The upper-cone, also called the future light-cone, defines the future description of a light-flash discharged at the event. The lower-cone, also called the past light-cone, describes all directions from whatever light-flashes can be collected at the event. 5

Lyman-alpha (Lyα) line Spectral line of one-electron ions, in particular hydrogen, in the Lyman series. This line is emitted when the electron falls from second principal quantum number (n) to $n = 1$. 5

Nasmyth Platforms Ultra-stable platform suitable for high-resolution spectrographs mounted at alt-azimuth telescopes. 15, 18

Phantom Energy Fields Proposed by Caldwell in [1], a phantom energy field is a scalar field with negative kinetic energy to study the possibility of a late acceleration in time with an equation of state parameter $w < -1$. 9

Quasi-Stellar Object Quasi-Stellar Object (QSO), also known as quasar, is an extremely luminous AGN. The quasars with greater luminosity can reach luminosities thousands of times superior to the luminosity of a galaxy like the Milky Way. These celestial objects are the most common subclass of AGN. These characteristics make quasars the brightest stable sources of electromagnetic radiation in the universe. 5

Acronyms and Initialisms

ΛCDM Λ Cold Dark Matter xv, xvi, xvii, 4, 9, 27, 29, 30, 31, 32, 34, 36, 39, 46

AGN Active Galactic Nuclei xix, xx, 5
ANDES ArmazoNes high Dispersion Echelle Spectrograph ix, xi, xv, xvii, 1, 2, 7, 8, 17, 18, 19, 21, 23, 25, 27, 35, 36, 47
APSU Anamorphic Pupil Slicer Unit 16

BBO Big Bang Observer 19

CAUP Centro de Astrofísica da Universidade do Porto 1, 2
CCD Charge-Coupled Device 17
CCL Combined-Coudé Laboratory 15, 16
CMB Cosmic Microwave Background 7
CMBR Cosmic Microwave Background Radiation 4
CODEX Cosmic Dynamics and Exo-earth Experiment 18
CPL Chevallier-Polarski-Linder xv, xvi, xvii, 9, 10, 29, 32, 33, 34, 35, 38, 39, 40, 42, 43, 44, 45, 46

DECIGO Deci-hertz Interferometer Gravitational Wave Observatory 19

ELT Extremely Large Telescope ix, xi, 1, 2, 7, 17, 27, 29
ESO European Southern Observatory ix, 1, 17
ESPRESSO Echelle SPectrograph for Rocky Exoplanets and Stable Spectroscopic Observations xv, xvii, 1, 7, 15, 16, 17, 18, 19, 21, 47

FITS Flexible Image Transport System 22
FLRW Friedman-Lemaître-Roberson-Walker 4, 9
FoM Figure of Merit xv, 25, 29, 30, 31, 32, 33, 34, 36, 37, 40, 44
FP Fabry-Pérot 16
FWHM Full Width at Half Maximum 23

GTO Guaranteed Time Observations 47

HARPS High Accuracy Radial velocity Planet Searcher 7, 15
HWHM Half Width at Half Maximum 22

Keck-HIRES High Resolution Echelle Spectrometer of the Keck telescope 7

LDLS Laser-Driven-Light Source 16
LFC Laser-Frequency Comb 16

QSO Quasi-Stellar Object xx, 5, 6, 19, 21, 22, 27, 28, 29
QUBRICS QUasars as BRIght beacons for Cosmology in the Southern hemisphere 28

RMS Root-Mean-Squared 22

S/N Signal-to-noise Ratio 17, 19
SKAO Square Kilometer Array Observatory 19, 29, 30, 31, 32, 33, 34

ThAr Thorium-Argon hollow-cathode lamp 16

UT Unit Telescope 15, 16
UVES Ultraviolet and Visual Echelle Spectrograph 7, 15

VLT Very Large Telescope 1, 15, 17

Chapter

1 Introduction

1.1 Motivation

Whether in terms of instrument design or construction or in terms of scientific planning and exploitation, Portugal, and in this particular case Centro de Astrofísica da Universidade do Porto (CAUP), are strongly entangled in European Southern Observatory (ESO) instrumentation programs.

It would not be correct to speak individually of CAUP's participation in design and construction, as they do not exist by themselves, they are interconnected with scientific planning. These two are not independent because the instruments are constructed with well-defined scientific purposes, but are then subject to several financial and technical restrictions. On the other hand, scientific exploitation programs must be optimized taking into account the instrument's specifications.

One of the research fields in which CAUP is highly involved is the high-resolution spectroscopy tests of fundamental physics, such as those carried out at ESO facilities. CAUP contributed to the construction of the Echelle SPectrograph for Rocky Exoplanets and Stable Spectroscopic Observations (ESPRESSO) instrument, recently installed in the Very Large Telescope (VLT) Coudé laboratory in Chile. Currently it is involved not only in the scientific exploitation of ESPRESSO but also in the development of its successor for the Extremely Large Telescope (ELT), the ArmazoNes high Dispersion Echelle Spectrograph (ANDES).

The ANDES instrument, currently starting its phase B of construction, will enable scientific research in several astrophysical areas. This powerful spectrograph will allow astronomers to search for and describe planets outside our solar system and identify vestiges of the first generation of stars that made up the primitive universe. In addition to astronomy, ANDES will reach the field of fundamental physics, where this thesis is based. In this field, it will help to determine whether some of the fundamental constants of physics, which regulate most of the physical mechanisms in the Universe, vary with space and time. In particular, with ANDES we will achieve more accurate tests of the fine-structure constant and the electron-proton

mass ratio. Furthermore, the main driver of ANDES science and design is the measurement of redshift drift. This direct and independent measurement of the universe's expansion model will constitute evidence of the acceleration of movement of celestial objects according to Hubble's law. So, we can say that this instrument will have a great impact on our understanding of the universe and its evolution.

This thesis is a contribution to Phase B of the construction of ANDES and focuses on some of the tasks in the field of fundamental physics assigned to the CAUP team.

1.2 Objectives

This thesis has great emphasis on programming, optimization, modulation, simulation (including the creation of simulated data) and data analysis (including its visualization). The main objective is to develop and improve computational tools that can optimize ANDES observations for the scientific case of astrophysical tests of fundamental physics (covering measurements of the redshift drift and the value of the fine-structure constant), for possible and feasible instrument configurations.

Based on the knowledge of the CAUP team with the ESPRESSO spectrograph, we will generate realistic simulated datasets for the distinct specifications of ANDES. Through these simulations, we will be skilled to analyze the scientific impact on the various possible configurations of the instrument. Thus, we will recognize the crucial parameters for the indispensable scientific compensations.

Divided into three important sections, this thesis starts with the development of all the code needed for modeling and simulating realistic data sets for various ANDES specifications, in particular in redshift drift and fine-structure constant measurements. The next section focuses on the scientific analysis of the trade-offs of the possible instrument configurations. This analysis makes it possible to quantify the scientific impact of each instrument configuration. And as a consequence, the identification of key parameters for scientific trade-offs. In the last section, the ANDES and consequently ELT would already be in its Phase B construction. Since they are not in Phase B, the last section focuses on quantifying the agreement of our models with the data.

This type of study is crucial for phase B of the construction of the instrument, since ultimately it will lead to the definition of an optimized observation method, which is the starting point for the subsequent planning of the scientific exploitation of the instrument. It is at the end of Phase B that the entire instrument design is defined. That is why it is very important to ensure that all options have been explored before final decisions are made.

CHAPTER

2 State of the Art

Cosmology is one of the branches of physics and an experimental science that combines theoretical predictions with observable data, comparing them. Bearing in mind that this comparison is frustrated by the experimental and instrumental limitations that influence and thus modify the astronomical data.

In 1922, Alexander Friedmann formulates Friedmann's Equations, deriving the first solutions to Einstein's equations for an expanding universe [2]. Five years later, Georges Lemaître derived a non-static solution to Einstein's equations and coupled it with the observations then available to suggest a possible, but inconclusive relationship between speed and distance, which would be expected for the non-static universe [3].

In 1929, Edwin Hubble detected that the distance of a galaxy is approximately proportional to its redshift [4]. The term redshift, possibly observed and described for the first time by Walter S. Adams, was then confirmed by Hubble. He further formulated what we know as Hubble's Law, given as

$$v = H_0 \times d, \tag{2.1}$$

where v is the recession velocity, d the distance of a galaxy and H_0 is called the Hubble constant, the present-day value of the Hubble parameter.

This law shows us that the farther a galaxy is, the faster it recedes. This has become proof that our universe is expanding, as studied by Friedmann and Lemaître. The proportionality constant, the Hubble constant H_0, describes the current rate of cosmic expansion generated by the elongation of the space-time itself. Although H_0 is designated as a constant, it changes with time.

Despite the apparent similarities to the Doppler shift, redshift has a slight distinction. In Doppler shift, the movement of the object at the instant the photons are emitted influences the wavelength of the radiation emitted by this object. If it is moving towards us, the wavelength is shifted to the blue area of the spectrum. In contrast, if it moves in the opposite direction, the wavelength is shifted to red. Redshift, z, can be characterized as the stretching of the

wavelength of light and therefore the light is shifted in the direction of the longer wavelengths, that is, the red part of the spectrum and defined as

$$z = \frac{\lambda_{\text{obs}} - \lambda_{\text{emit}}}{\lambda_{\text{emit}}}, \tag{2.2}$$

where λ_{obs} is the wavelength of the light observed from some object and λ_{emit} is the wavelength of the light emitted by the same object.

In other words, redshift results from the expansion of space itself and not from the movement of a body. Therefore, two galaxies can be static in space and nevertheless experience a redshift if the middle space itself is increasing.

In the late 1940s, George Gamow, Ralph Alpher and Robert Herman theoretically postulated the existence of Cosmic Microwave Background Radiation (CMBR). Through the study of the synthesis of light elements, they realized that the Universe in its initial moments needed to be extremely hot. The radiation from this "hot Big Bang"still remains in our universe and would be detectable today as CMBR. With the expansion of the Universe, they estimated that the current temperature of the universe would be 3 K, which corresponds to the microwave wavelengths. This radiation was only detected for the first time in 1964 accidentally by Arno Penzias and Robert Wilson.

We can define a new era of cosmology made possible by observational advances and based on the first observations of the expanding universe and on the CMBR, the era of modern cosmology. The accumulation of observations has led to a rejection of some theoretical predictions and the improvement of others. With all improvements it was possible to arrive at a standard parametrization of our Universe, called Λ Cold Dark Matter (ΛCDM) model.

The ΛCDM model - the simplest available model consistent with observations - is based on the Friedman-Lemaître-Roberson-Walker (FLRW) equations, solutions of Einstein's equations of General Relativity that describe the spatially homogeneous space-time in expansion or contraction. This standard 6-parameter model assumes that the universe is composed of photons, neutrinos, common matter (baryons and leptons), cold dark matter (not relativistic - that only interacts gravitationally) and dark energy. It was then set one of the main paradigms of cosmology where our universe is monopolized by two unexplained elements - dark matter and energy. Both were discovered statistically in cosmological and astrophysical observations, but have not yet been discovered experimentally (i.e., in the laboratory).

Dark matter is responsible for the formation of the structure of the universe. The cosmological constant, Λ, in the ΛCDM model is correlated with the energy density of the vacuum and this density is associated with dark energy. This constant is the simplest explanation and consistent with the data available for the acceleration source of the universe and its origin.

By the year 1962, Sandage and McVittie were the first to point out that, due to the cosmological expansion, the redshift of astrophysical objects varies with time - a phenomenon known as redshift drift. As demonstrated by Martins in [5], the redshift drift of an object that follows the cosmological expansion and in a given time interval, Δt, can be given by

$$\frac{\Delta z}{\Delta t} = H_0[1 + z - E(z)], \tag{2.3}$$

where $E(z)$ is the rescaled Hubble parameter that can be expressed as $E(z) = \frac{H(z)}{H_0}$.

Theoretically astrophysical spectroscopy provides us with a simple technique for measuring redshift drift and even quite intuitive. With the astrophysical observations made so far, we can map our present-day past Light Cone, the lower cone in figure 2.1. By contrasting distinct past Light Cones (distinct bottom cones), we could observe the universe expand in real time, reaching then the redshift drift. This technique, in particular, is independent of assumptions on any model of expansion of the universe and does not even require some sort of hypothesis on clustering, geometry or gravitational behavior. The obstacle with this technique lies in the cosmological timescales involved. These timescales are far superior to human timescales.

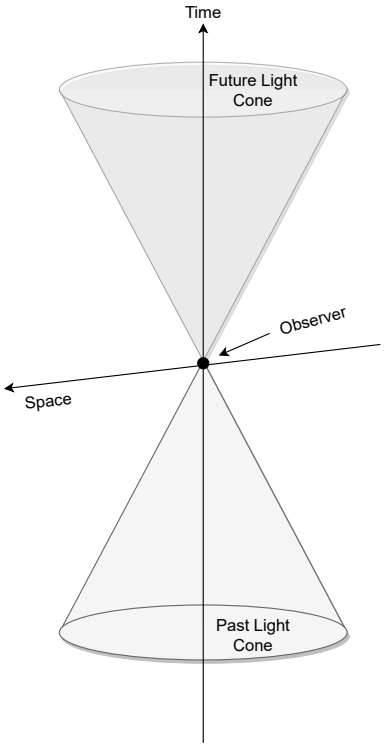

Figure 2.1: Representation of light cones.

Years later, Loeb (1998) mentions several astrophysical systems for the measurement of redshift, in particular through the use of the Lyman-alpha forest, which he called the Sandage-Loeb test. The Lyman-α forest is an absorption phenomenon detected in the spectrum of high redshift of galaxies and Active Galactic Nuclei (AGN) objects such as Quasi-Stellar Object (QSO).

Quasars radiate electromagnetic radiation of nearly unvarying intensity over an ample wavelength range. This brightness and invariant intensity in their spectra allows to measure the absorption lines caused by the matter along the line of sight between the observer and the quasar. Starting at the wavelength of the QSO's own emission Lyman-alpha (Lyα) line and stretching blueward, all QSO at large redshift display extensive numbers of slim absorption lines.

As we can see in figure 2.2, from the Lyα absorption line and stretching blueward (the left side of the absorption line), we identify a large number of other absorption lines. This series of absorption lines is called the Lyman-α forest.

By subtracting two spectra from the same quasar with a considerable time difference, for example 10 years or even more, we will obtain the values of redshift drift, since the redshift varies with time.

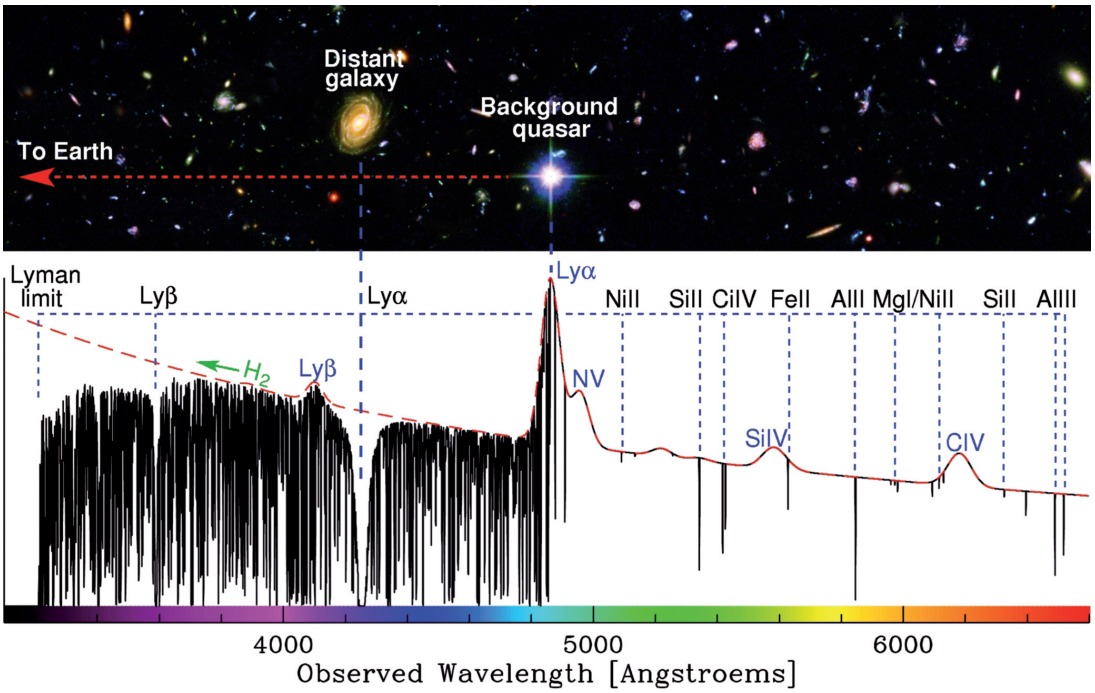

Figure 2.2: The quasar absorption line experiment. Retrieved from [6]

The absorption spectra of the quasars (like the one shown in figure 2.2) are also strong resources for testing the variation of the dimensionless fundamental parameters. As studied by Uzan in [7], a fundamental constant of a certain physical theory is a parameter whose value cannot be explained by the theory itself, only by measurement. To test a theory, we study the invariability of the fundamental constant, both in the primitive universe by cosmological observations and in the laboratory. And so we are able to determine its validity domain. If its constancy is evaluated as not valid, we can interpret it as a clue to a new physics.

On the right side of the Lyα absorption line in figure 2.2, the quasar spectra show some lines of metal absorption. These lines may be associated with clouds of the materials of the galaxy that hosts the QSO or correspondent to diverse celestial objects at other cosmological distances that are in the identical line of sight. These absorption lines are sensitive to the variation of the fundamental parameter, the fine-structure constant (α). In particular, each metallic element has a different sensitivity to it. This variation will imply a violation of the Einstein Equivalence Principle, questioning the only four forces of nature and the rupture of gravity as Uzan describes in [7].

The fine-structure constant, the "coupling constant", measures the strength of the electromagnetic force that describes how electrically charged elementary particles and photons interact. At the observational level, we can define the variation in α as

$$\frac{\Delta\alpha}{\alpha}(z) = \frac{\alpha(z) - \alpha_0}{\alpha_0}, \tag{2.4}$$

where $\alpha(z)$ is the measurement of α at some redshift z and α_0 is the laboratory value of α.

In recent years, several observational feasibility studies have been carried out so that high resolution spectrographs could make better measurements of the redshift drift and α. High Accuracy Radial velocity Planet Searcher (HARPS), Ultraviolet and Visual Echelle Spectrograph (UVES) and High Resolution Echelle Spectrometer of the Keck telescope (Keck-HIRES) were built for these purposes. In addition to these, ESPRESSO was also built, the main predecessor of ANDES, which will be installed at the ELT.

The ESPRESSO is an ultra-stable, high-resolution spectrograph from the Very Large Telescope. This spectrograph combines the high spectroscopic precision with the efficiency of a modern Echelle spectrograph with extreme radial speed. It is installed in the Combined Coudé Laboratory of the VLT and also has the advantage of being connected to four Unit Telescopes (UT) which allows operations with only one UT or with the four UTs. Using the 4UT mode, it is possible to make slightly less accurate measurements from fainter sources than those from the 1UT, which allows higher redshift objects to be observed. One of the main points of the construction and theoretical bases of this spectrograph is the performance of tests with greater precision of the stability of nature's fundamental couplings, in particular the variations of the fine-structure constant, α.

A crucial limitation of ESPRESSO is its wavelength coverage amplitude, which is thinner than the ones of its predecessors. Adding to the fact that current installations only allow sensitivities some orders worse than the expected signal and redshift measurements require a very exquisite sensitivity, ANDES began to be designed.

In 2008, Liske et al. studied the feasibility of high redshift measurements with ANDES [8]. In 2012, Martinelli et al. quantify the impact of combining ANDES redshift measurements with standard Cosmic Microwave Background (CMB) data [9]. Revealing that this combination leads to the breaking of the degeneracy of the expansion universe parameters, which implies a highly substantial improvement in the cosmological constraints.

On the other hand, it is also possible to measure redshift drift using CMB data. This type of measurement requires a century-long time scale, as studied by Lange and Page [10]. The need for an experiment time scale of one century when looking at the CMB comes from the fact that we are looking at very high redshifts, and therefore need a long time to observe a statistically different past light cone.

Although all these studies with redshift drift measurements with ANDES do not lead to stricter cosmological parameters restrictions than those available with the usual probes, CMB or supernovae, these redshift drift measurements probe regions of parameter space that are

different from the usual ones. Therefore, and in combination with the currently known restrictions, we will arrive at much stricter combined restrictions. Discussed in further detail in 2019 by Alves et al. [11].

In this work we will present the analysis of realistic simulated datasets that influence the possible configurations of the ANDES spectrograph. And so, we will know what are the optimal instrumental parameters for maximizing the instrument's scientific impact. For this purpose, two different software tools should in principle be used that will complement each other.

In the first approach and through several inputs such as real quasar file and the different properties of the instrument (for example wavelength range, efficiency or even experiment time), a code should be used to generate the quasar data. From these data, it would be possible to reproduce two separate spectra with a given time interval. Once the redshift of each absorption line is obtained, the redshift drift and respective error bars are easily calculated. Since ANDES Phase B has not started yet, will use simplified assumptions for this part.

In second analysis, another type of code will be used that will allow us to explore cosmological constraints from the data we obtained with the previous software tool. The Fisher Matrix Analysis code, [11], takes as input the error bars of redshift drift measurements and will let us predict the cosmological impact of these astrophysical tests, which could lead to new constraints on the cosmological parameters that describe our universe.

2.1 Fiducial Models of our Universe

The observations made so far suggest that the universe is controlled by an energy component, similar to the behavior of a cosmological constant from a gravitational point of view. Consistent with the available data, a cosmological constant will have to take on a smaller value than particle physics expectations. [12] Thus, a dynamical scalar field becomes a plausible alternative. With pressure of the field $p < 0$ and the accelerated expansion of the Universe, the field should be slow-rolling, since the physical regime responsible for the acceleration of the Universe is now dominating the dynamics of the acceleration. The field will couple to the rest of the model, leading to long-range forces that will be possibly observed and time dependencies of the nature constants.

A coupling to the electromagnetic sector is going to lead to space-time variations in the fine-structure constant α. Stability tests of fundamental couplings will therefore be crucial to the constraint on both fundamental physics and fundamental cosmology. Whether the test results are null or some variation is detected, both will have a great importance. Null results of variations will correspond to the normal expectation for these. In contrast, any detectable variations will lead to an improved constraint on the fundamental cosmology. We guarantee that any theoretical constraint will only be influenced by the sensitivity of the tests.

We can divide the scalar field based models for variable couplings into two broad classes. Class I covers all models in which a single new dynamical degree of freedom accounts for both variable constants and dark energy. In this class of models, the redshift dependence of the couplings is determined parametrically. The measurements achieved will be employed as

a way to establish constraints on the combinations of the scalar field coupling and the dark energy equation of state. The relative variation of α in these models is given by:

$$\frac{\Delta\alpha}{\alpha}(z) = \zeta \int_0^z \sqrt{3\Omega_\phi(z')[1+w_\phi(z')]}\frac{dz'}{1+z'}, \tag{2.5}$$

here ζ is the coupling of the scalar field to the electromagnetic sector of the theory (dimensionless), w_ϕ is the dark energy equation of state and $\Omega_\phi = \rho_\phi/(\rho_\phi + \rho_\mathrm{m})$ is the fraction of the energy density of the universe.

Equation 2.5 assumes a canonical scalar field, with $w_\phi \geq -1$. However, the argument can be repeated for Phantom Energy Fields [13] as:

$$\frac{\Delta\alpha}{\alpha}(z) = -\zeta \int_0^z \sqrt{3\Omega_\phi(z')|1+w_\phi(z')|}\frac{dz'}{1+z'}, \tag{2.6}$$

where the negative sign derives from the fact that we expect a phantom field rolls up the potential instead of rolling down.

From FLRW equations, one of the well-known parametrizations of the dark energy equation of state, is the Chevallier-Polarski-Linder (CPL) [14][15] parametrization, described by:

$$w_\mathrm{CPL}(z) = w_0 + w_\mathrm{a}\frac{z}{1+z}, \tag{2.7}$$

where w_0 is its present value and w_a is the coefficient of the time-dependent term. For this parametrization the square of the rescaled Hubble parameter is given by:

$$E^2(z) = \Omega_\mathrm{m}(1+z)^3 + \Omega_\Lambda(1+z)^{3(1+w_0+w_\mathrm{a})}\exp\left(-\frac{3w_\mathrm{a}z}{1+z}\right), \tag{2.8}$$

where Ω_m is the present time matter density and it was assumed a flat universe (i.e., $\Omega_\mathrm{m}+\Omega_\Lambda = 1$). Supposing that the dark energy is produced by a scalar field, coupled to the electromagnetic sector, we can describe the energy density fraction as:

$$\Omega_\mathrm{CPL}(z) = \frac{1-\Omega_\mathrm{m}}{1-\Omega_\mathrm{m}+\Omega_\mathrm{m}(1+z)^{-3(w_0+w_\mathrm{a})}\exp(3w_\mathrm{a}z/1+z)} \tag{2.9}$$

Figure 2.3 illustrates the behavior of $\Delta\alpha/\alpha(z)$ in this model for realistic choices of parameters. On the left is plotted $\Delta\alpha/\alpha(z)$ with $w_0 = -0.95$, $w_\mathrm{a} = 0.2$ and $-1\times10^{-6} \leq \zeta \leq 1\times10^{-6}$; on the right $\Delta\alpha/\alpha(z)$ with $w_\mathrm{a} = 0.1$, $\zeta = 5\times10^{-6}$ and $-1.1 \leq w_0 \leq -0.9$.

The CPL parametrization also has two particular cases, one of them used in this dissertation. The canonical ΛCDM, where $w_\mathrm{a} = 0$ and $w_0 = -1$, and the constant dark energy equation of state (w_0CDM), where $w_\mathrm{a} = 0$. For ΛCDM model, the square of the rescaled Hubble parameter is a limit of equation 2.8, where replacing w_0 by -1 and w_a by 0 we have:

$$E^2(z) = \Omega_\mathrm{m}(1+z)^3 + \Omega_\Lambda \tag{2.10}$$

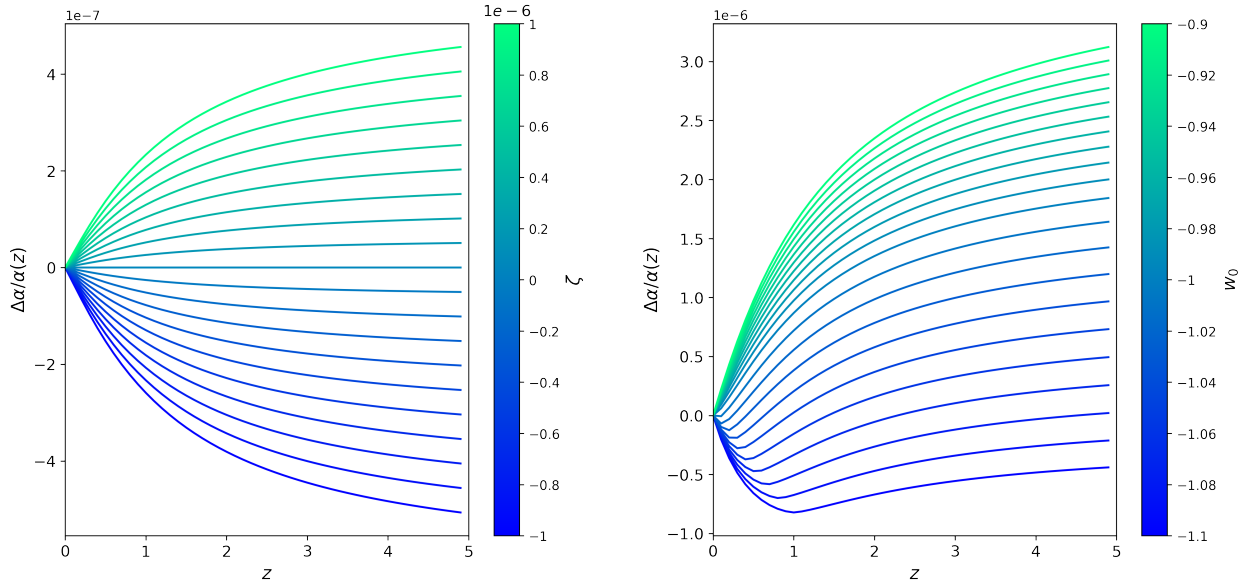

Figure 2.3: Relative variation of α with the relevant parameters of the CPL model.

On the other hand, Class II models are those in which the field providing the variable couplings does not provide the dark energy. Examples of models of this class include the Bekenstein-type models [16].

In Bekenstein-type models different couplings to the dark energy and matter sectors are allowed, and the behavior of α depends on both of them. One of the Bekenstein-type models was used in this dissertation. In this model, the relative variation of α is given by:

$$\frac{\Delta\alpha}{\alpha}(z) = 2\zeta_{\rm m}\log(1+z) + \frac{2(\zeta_\Lambda - 2\zeta_{\rm m})}{3\sqrt{\Omega_\Lambda}}\left[\log\left(\frac{1+\sqrt{\Omega_\Lambda}}{\sqrt{\Omega_{\rm m}}}\right) - \sqrt{E^2(z)}\log\left(\frac{\sqrt{\Omega_\Lambda}+\sqrt{E^2(z)}}{\sqrt{\Omega_{\rm m}(1+z)^3}}\right)\right], \tag{2.11}$$

where ζ_Λ and $\zeta_{\rm m}$ are the parameter combinations that are constrained by the astrophysical measurements of α. Furthermore, it was once again assumed a flat universe and the rescaled Hubble parameter used in this model is the one given by equation 2.10.

Figure 2.4 illustrates the behavior of $\Delta\alpha/\alpha(z)$ in this Bekenstein-type model for realistic choices of parameters. On the left is plotted $\Delta\alpha/\alpha(z)$ with $w_0 = -1$, $w_{\rm a} = 0$, $\zeta_{\rm m} = -0.78\times10^{-6}$ and $-5\times10^{-6} \leq \zeta_\Lambda \leq 5\times10^{-6}$; on the right $\Delta\alpha/\alpha(z)$ with $w_0 = -1$, $w_{\rm a} = 0$, $\zeta_\Lambda = 1.15\times10^{-6}$ and $-3\times10^{-6} \leq \zeta_{\rm m} \leq 3\times10^{-6}$.

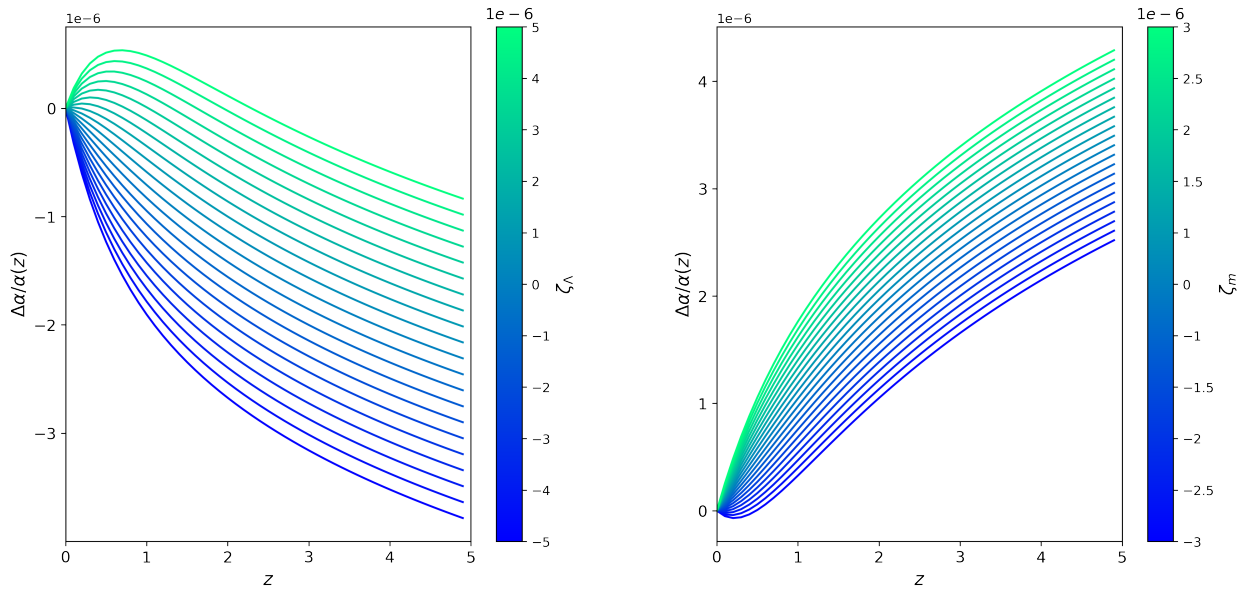

Figure 2.4: Relative variation of α with the relevant parameters of the Bekenstein-type model.

CHAPTER

3 High-Resolution Spectrographs

High-resolution spectrographs are the main core of astrophysics and therefore the basic observational tool for both stellar physics and the interstellar and intergalactic medium. With the increase and improvement of telescopes, spectrographs upgrade their capabilities, extending their high resolution to fainter celestial objects. The construction of a new telescope now has two prime goals, increasing the photon-collecting power and high-precision spectroscopy.

3.1 Echelle Spectrographs

An astronomical spectrograph disperses light from a source into its component wavelengths. This scattering is usually done through a diffraction Grating or prism.

In a diffraction grating, the incident light (composed of batches of distinct wavelengths) satisfies the equation 3.1, where the light components are diffracted at angles determined by the assigned wavelength.

$$d(\sin\alpha - \sin\beta) = m\lambda \tag{3.1}$$

Where α is the incident angle and β is the diffraction angle, both measured with the normal to the diffraction grating, d is the period of the grating, m is the diffraction order and λ is the wavelength.

For high-resolution spectroscopy, as the name implies, a higher resolution is required than for ordinary spectrographs. A grating suitable for this purpose is known as an echelle. Simply replacing the standard grating with an echelle leads to the overlap of several diffraction orders, particularly the higher orders. This overlap is due to the fact that the Free Spectral Range is considerably smaller. To overcome the effect of the overlap an extra scattering element, the cross-disperser, is used. This lower diffraction grating, the cross-disperser, will disperse light in the direction perpendicular to the dispersion direction of the echelle grating. This allows a wide wavelength coverage since the result of this scattering is a two-dimensional spectrum.

Becoming one of the great advantages of echelle spectrographs, the two-dimensional spectrum represents on its vertical axis the directions of dispersion by the cross-disperser and on the horizontal axis by the echelle. If the Free Spectral Range were fully covered by the detector a spectrum with the complete range of wavelengths and with no gaps would be achieved. That said, the choice of the cross-disperser must always take into account what number of orders and interval between them we would like to study, since this influences the observable region in the sky.

A cross-dispersed echelle spectrograph is schematized in figure 3.1. We can observe that light from a given source is incident on the echelle grating, where it will be scattered into wavelengths dispersed by the corresponding diffraction angles. However, wavelengths corresponding to different diffraction orders overlap spatially. To resolve this overlapping, the light passes through the cross-disperser that will scatter the light in the direction perpendicular to the direction in which the light is scattered in the echelle. The final spectrum will be a two-dimensional spectrum.

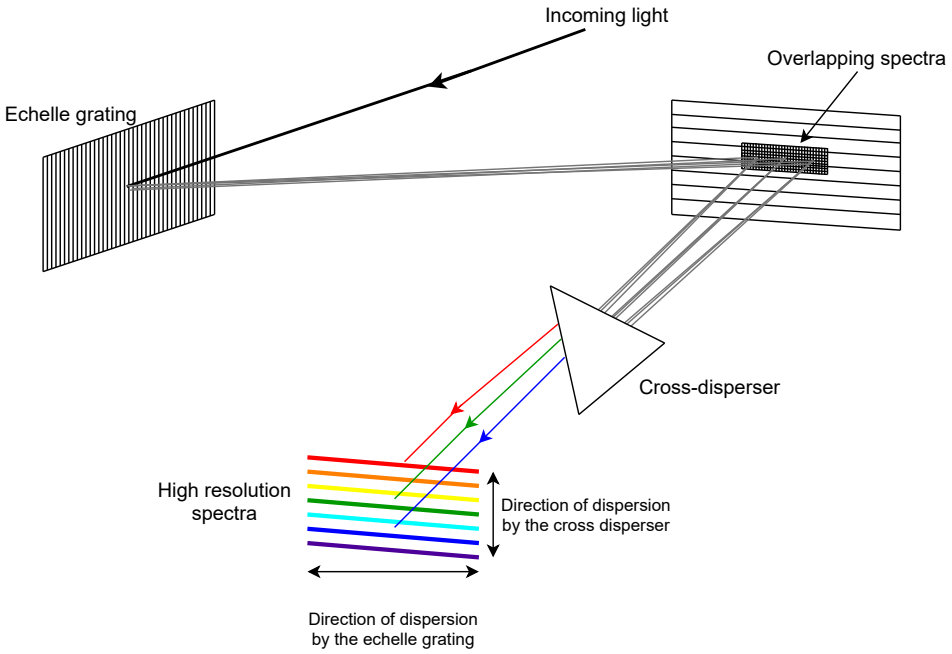

Figure 3.1: Schematic diagram of a cross-dispersed echelle spectrograph. Adapted from [17]

Echelle spectrographs can additionally be supplied by optical fibers (fiber-fed). These will be in charge of collecting the light from the telescope and directing it to the spectrograph. This provides two, much needed, advantages for telescope construction, the ease of moving a single fiber instead of dismantling the entire instrument, and the capability of obtaining simultaneous spectrums.

3.1.1 Echelle Spectrograph for Rocky Exoplanets and Stable Spectroscopic Observations - Very Large Telescope

Located on the Combined-Coudé Laboratory (CCL), ESPRESSO is the VLT's ultra-stable high-resolution spectrograph. Both in terms of technology and the design of the spectrograph itself, we can say that the ESPRESSO is the successor of the HARPS spectrograph. However, at the level of the type of telescope they are in (large telescopes) and the scientific objectives, in particular the application in cosmology, the ESPRESSO is considered as the successor of the UVES. The detection and characterization of Earth-like planets and the measurement of the possible variation of the constants of the Universe are the two major scientific goals of this highly stabilized fiber echelle spectrograph. Supplied by two fibers, one for the scientific target and the other one for simultaneous reference, ESPRESSO also has the particularity of being able to collect light from a single or up to four Unit Telescopes (UTs) at the same time.

Until it reaches the spectrograph itself, the light passes through three distinct subsystems of the ESPRESSO: the Coudé Train (CT), the Front Ends (FE) and the Calibration Unit (CU), as illustrated in figure 3.2.

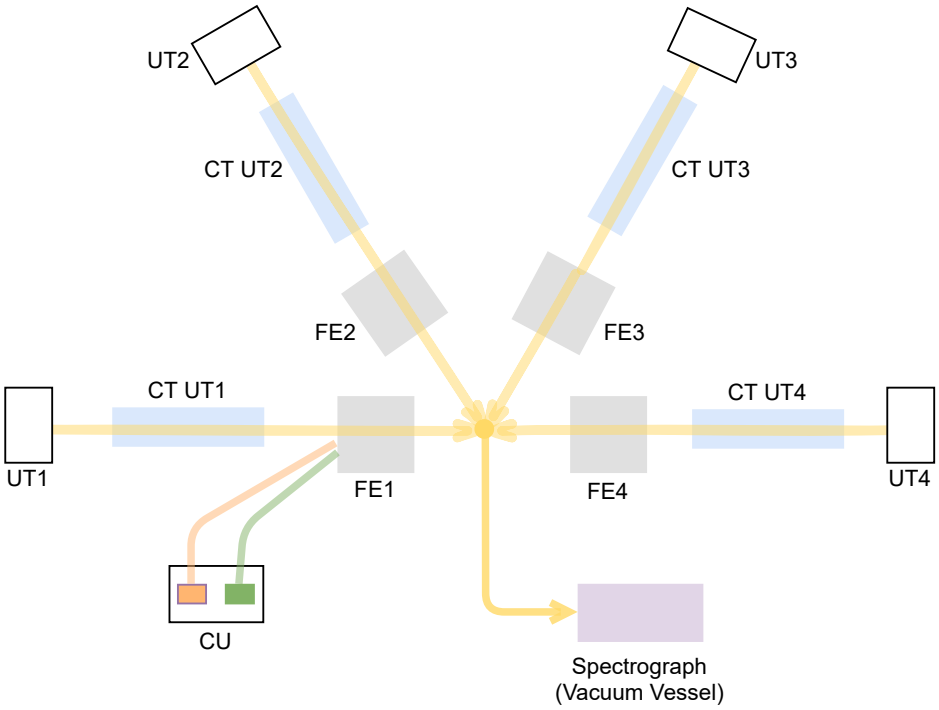

Figure 3.2: Schematic representation of ESPRESSO and its different subsystems. UT - Unit Telescope; CT - Coudé Train; FE - Front End; CU - Calibration Unit. The numbers refer to the Unit Telescope used. Adapted from [18].

The redirection of the light from the telescopes (just one or even a combination of all four) to the CCL is performed by the Coudé Trains. The light is captured by the Coudé Trains at the Nasmyth Platforms level and redirected to the Coudé Rooms through an optical system composed of several optical elements such as prisms, mirrors, lenses, and fibers. Guided by

the incoherent light tunnels, the beams from the four UTs meet at the CCL, where the mode setting and beam conditioning will be done by the Front-End subsystem.

The Front-End subsystem consists of the rigid frame assembly with four arms, each arm oriented toward the incoherent light tunnels of the respective UT. Each beam received by the associated Coudé Train is corrected through an Atmospheric Dispersion Correction unit, where it is redirected to a common focal plane. This focal plane is also where the fiber feed to spectrograph is processed. The Front-End is further responsible for injecting either into the fibers or into the spectrograph the calibration light. Thus, we can simply describe the Front-End as the necessary connection between the input signal (i.e., object light, sky light and calibration light) and the output fiber. The Fiber-Link is responsible for the re-transmission of light from the Front-End to the spectrograph in the vacuum vessel and also for performing the essential task of light scrambling. By scrambling the light, a homogeneous light distribution will be ensured and will minimize the negative effects of not only atmospheric turbulence but also a weakly centered target. This makes the obtained spectra very insensitive to variations in the distribution of incident light.

The Calibration Unit, as the name suggests, is a set of devices that allow the correct calibration of the instrument. When daily calibrations are performed, only one of the Front-Ends will be supplied with this calibration light that will transmit to the other UTs in order to provide a common reference calibration, as shown in figure 3.2. ESPRESSO is equipped with different calibration sources. A Fabry-Pérot (FP) to perform a wavelength calibration over the entire spectral range, characterized as a cavity illuminated with white light and is used for simultaneous reference measurements. And a Thorium-Argon hollow-cathode lamp (ThAr) is used for wavelength calibrations in regular studies and can be used in combination with an FP to extend and improve this calibration. For absolute calibration, the ESPRESSO also has a Laser-Frequency Comb (LFC) that is intended to perform a more accurate calibration at wavelengths between 500 and 720 nm. Lastly it is also equipped with a Laser-Driven-Light Source (LDLS) used for location, profile, and spectral flat-field calibration.

In order to achieve the high precision required in the measurements, ESPRESSO is mounted in a vacuum vessel so that a pressure of the order of 10^{-5} mbar is maintained during its operation. To avoid deviations in the temperature at which the instrument is working, a multi-shell thermal enclosure system has been developed so that the temperature is stabilized in the order of mK.

Figure 3.3 reveals the optical sketch of the spectrograph. The beam enters through the Anamorphic Pupil Slicer Unit (APSU) which will compress the beam in the cross scattering direction and the pupil slicer will split the pupil into two beams. These are then superimposed on the echelle grating, which will scatter the beam to the Dichroic Filter that separates it into a blue and a red spectroscopic arm, as can be noted in the figure. This division, in blue and red arms, allows both greater optical efficiency and better quality in the resulting image at each arm. Forwarded to the cross-disperser, the beams will be separated in all their spectral orders that were overlapping, as explained in section 3.1. To maximize the space between the orders an anamorphism is again introduced to reshape the pupil to a square. This will imply

an increase in the Signal-to-noise Ratio (S/N) for each pixel. Finally, each light beam reaches the respective Charge-Coupled Device (CCD), where it is registered. Between 380 and 525 nm the light is registered on the blue CCD, and between 525 and 788 nm on the red.

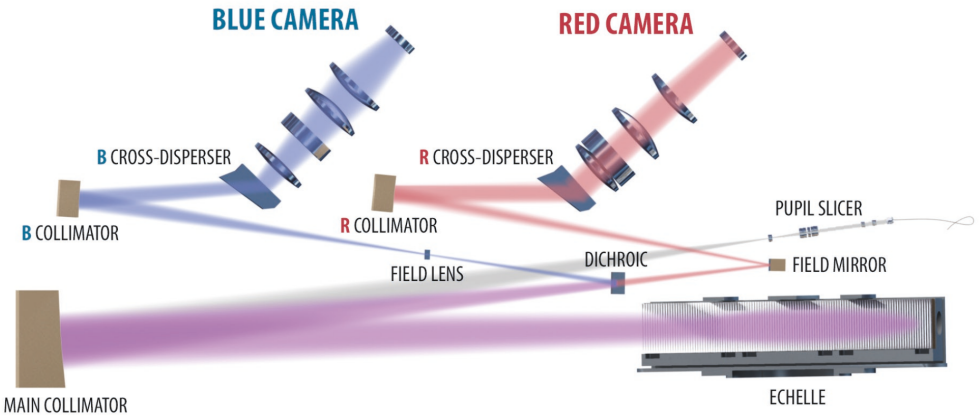

Figure 3.3: Schematic diagram of the optical components that belong to the ESPRESSO. Retrieved from [18].

ESPRESSO can be operated in three different observation modes: High Resolution 1-UT (HR), Ultra High Resolution 1-UT (UHR) and Medium Resolution 4-UT (MR). Their differences are summarized in table 3.1.

Table 3.1: Main characteristics of ESPRESSO observation modes. Retrieved from [18].

	HR (1-UT)	**UHR (1-UT)**	**MR (4-UT)**
Wavelength Range	380 – 788 nm	380 – 788 nm	380 – 788 nm
Resolving power (median)	140 000	190 000	70 000
Aperture on sky	1".0	0".5	4x1".0
Total efficiency	11%	5%	11%
RV precision (requirement)	<10 cm/s	<5 m/s	<5 m/s
Limiting V-band magnitude	~17	~16	~20
Binning	1x1, 2x1	1x1	4x2, 8x4
Spectral sampling (average)	4.5 px	2.5 px	5.5 px (binned x2)
Spatial sampling per slice	9.0 (4.5) px	5.0 px	5.5 px (binned x4)
Number of slices	2	2	1

3.1.2 ArmazoNes high Dispersion Echelle Spectrograph - Extremely Large Telescope

Under construction at Cerro Armazones in Chile's Atacama Desert, the ELT is ESOs ambitious new program. And similar to the VLT, the ELT will also be equipped with a very powerful high-resolution optical spectrograph, the ANDES. Among the various scientific goals of ANDES, for this dissertation, we highlight not only the study of possible variations of the fundamental constants of physics (particularly the fine-structure constant) but also the direct measurement

of the expansion of the universe. At the time of writing this dissertation, ANDES has completed the initial phase of the project known as Phase A. Therefore, the description of the general characteristics and design of the ANDES spectrograph in this subsection will all concern what was established by Phase A.

This class of high-resolution spectrographs requires an extremely large photon collection area. And in view of this type of defined instrumentation two studies have been carried out, Cosmic Dynamics and Exo-earth Experiment (CODEX) [19] in the optical wavelength range and SIMPLE [20] in the near-infrared. The combination of the two studies demonstrated the enormous scientific significance of the telescope, and in particular the spectrograph, in covering the entire optical and near-infrared spectral range. This led to the development of the ANDES concept as we know it in the present, a spectrograph that both in terms of scientific goals but also technology and design is considered the successor of the ESPRESSO.

The basic idea behind ANDES is a modular instrument consisting of three ultra-stable and modular fiber-fed cross dispersed echelle spectrographs. The three spectrographs VIS-BLUE (visible-blue), VIS-RED (visible-red) and NIR (near-infrared) will be suitable to cover a wavelength range from 0.4 to 1.8 μm (goal 0.35 - 1.8 μm) with a spectral resolution power of $R \sim 100,000$ for a unique object. In figure 3.4 we can see the schematic representation of the ANDES spectrograph. Through Dichroic Filters, the light coming from the Front End is split into three channels of distinct wavelengths. Each of them will feed the corresponding spectrograph module via the fiber bundle associated with the channel. Moreover, each fiber bundle will correspond to a particular observation mode. In order to ensure stability for the required measurements, the three spectrographs, VIS-BLUE, VIS-RED and NIR, all have a fixed configuration. It is intended that all components of ANDES be placed on the Nasmyth Platforms, if possible due to their mass and volume. If this is not possible, the VIS-RED and NIR modules can be placed in the Coudé Room, where the Calibration Unit will also be located.

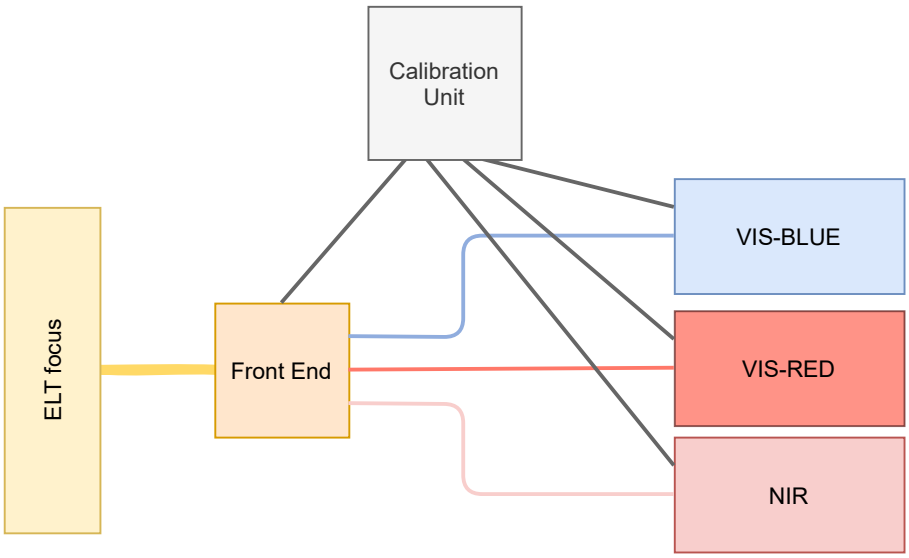

Figure 3.4: Schematic representation of ANDES. Adapted from [21].

Table 3.2 summarizes the characteristics defined by Phase A of ANDES. At this stage these are not the final characteristics of the instrument, as it may still suffer minor changes only if these are scientifically well justified.

Table 3.2: Main characteristics of ANDES.

Wavelength	0.40 – 1.80 μm (baseline), 0.33 – 2.44 μm (goal)
Spectral resolution	100 000 – 150 000
Field(s)-of-view	0.170", 64 fibers (R ∼ 100 000), 0.113", 96 fibers (R ∼ 150 000)

ANDES will have the strong advantage over ESPRESSO of covering the wavelength range of the near-infrared, allowing the range of measurements of α over and above $z = 4$. The feasibility of which has been recently demonstrated in [22]. For the common objective of spectrographs, the measurement of a possible variation of the fundamental physical constant α, we know in advance that ANDES should, at higher values of S/N, confirm the ESPRESSO results and take these into account for its observation plan. That said, we can predict two distinct possible scenarios:

- ESPRESSO does not detect any α variation. The tighter limits achievable by ANDES will constrain physics related to the unexplained elements of the universe, dark energy and dark matter. The redshifts of interest might differ from those initially predicted, or depend on new cosmological results (e.g., from the Euclid space mission).

- ESPRESSO detects the α variation. ANDES will map this variation across its range of attainable redshift and distinct environments.

For the other scientific goal of ANDES studied in this dissertation, the measurement of redshift drift, the major observational challenge for measuring redshift drift is to be expected to have an extremely small drift rate, $\sim$ 6 cm s^{-1} decade^{-1} at $z = 3$, as studied by Liske et al. in [8]. Using the Lyα forest of QSO absorption lines as a target, ANDES should be the first to have the power to respond to this challenge. Combining these results with those from the Square Kilometer Array Observatory (SKAO) radio telescope at $z < 1$ (in emission) and possibly at $z > 8$ (in absorption) [23] and probably gravitational wave observatories such as Deci-hertz Interferometer Gravitational Wave Observatory (DECIGO) and Big Bang Observer (BBO) at $z \sim 0.5$ (if feasibility is confirmed) will allow us to have a direct measurement of the expansion of the universe.

CHAPTER

4 Simulations and Cosmological Constraints

Bearing in mind all the similarities between the ESPRESSO and ANDES spectrographs presented in chapter 3, it is important to emphasize that all the knowledge gained from the predecessor spectrograph is used for the development of ANDES. In this chapter, we briefly discuss how simulated data is generated and how from this data we are able to achieve cosmological constraints on the parameters.

4.1 Generation of simulated data

As explained in chapter 2, QSO's at high redshifts exhibit the Lyman-alpha forest in the region to the left of the QSO's Lyα emission line, while on its right they exhibit metal absorption lines. Based on these characteristic spectra, the code necessary to perform the astrophysical tests of fundamental physics (specifically the measurements of the redshift drift and the value of the fine-structure constant) was developed.

A cloud, either in the same line of sight or in the galaxy that hosts the QSO, imprints absorption lines in the quasar's spectrum, which reveal the properties of the cloud itself. These lines can appear very close or even superimposed on each other (line blending). For this reason, the most appropriate way to get information about the characteristics of the clouds present is by modelling and adjusting each absorption line. A natural broadening, as an effect of the finite radiative lifetime, and a collisional/pressure broadening, as an effect of the finite lifetime of the quantum state owing to collisions, are present in each absorption line. These two broadenings are described by a Lorentzian profile. The absorption lines also experience a Doppler broadening, as a result of the thermal motion, which can be described by a Gaussian profile. Therefore, each absorption line is commonly fitted to a Voigt profile which is the convolution of the Gaussian $G(x;\sigma)$ and Lorentzian $L(x;\gamma)$ profiles, and empirically defined

as:

$$V(x;\sigma,\gamma) = \int_{-\infty}^{\infty} G(x';\sigma)L(x-x';\gamma)dx', \tag{4.1}$$

where $G(x;\sigma) = \frac{1}{\sigma\sqrt{2\pi}} \exp\left(-\frac{x^2}{2\sigma^2}\right)$ and $L(x;\gamma) = \frac{\gamma/\pi}{x^2+\gamma^2}$. Here σ is the standard deviation of the Gaussian profile, γ is the Half Width at Half Maximum (HWHM) of the Lorentzian profile and x is related to frequency and given by $x = v - v_0$, where v_0 is the line centre.

For our case study, the Voigt profile of a certain transition is described by a set of fixed and free parameters. As fixed parameters (determined empirically in the laboratory) we will have, for example, the inverse of the transition lifetime Γ and the rest wavelength λ. Determined by the models that fit the data, the free parameters can be the redshift z and the column density of the gas N. As additional and equally free parameters is included the variation in α $(\Delta\alpha/\alpha)$ and the gas temperature T. It is important to mention that the redshift, $(\Delta\alpha/\alpha)$ and temperature are constant values for all transitions observed in each cloud under study.

Written in Fortran and developed to fit diverse Voigt profiles to spectral data, the VPFIT program [24] is the most used tool for this purpose and also for $(\Delta\alpha/\alpha)$ measurements. The user must enter the data and the model that will be used, in a .13 file, with the parameters of the Voigt profiles, initial values for the free parameters and additional parameters such as the continuum and zero-level corrections. The VPFIT uses a nonlinear least-squares algorithm to find the Voigt profile fitting the experimental data. Associated with the fitting process, the error between the Voigt profile and the experimental one is minimized, which is quantified as:

$$\chi^2 = \sum_{\mathrm{i}=1}^{N} \frac{(F_{\mathrm{i}}^{model}(x) - F_{\mathrm{i}}^{data})^2}{s_{\mathrm{i}}^2}, \tag{4.2}$$

where χ^2 is the chi-square, x is the vector of initial values of the free parameters, F_{i}^{model} is a fit value at i and s_{i} is the Root-Mean-Squared (RMS) noise estimated there. When normalized χ^2, $\chi^2_\nu = \chi^2/\nu$ (ν is number of degrees of freedom), takes a value around a unity we consider the fit to be statistically acceptable. Which means that the dispersion of the data around the model predictions is consistent with the uncertainty about the data. Although reliant on the free parameters chosen by the user, the VPFIT has already been shown to produce reliable results on simulated data [25] [26] in the various tests that it has been subjected to over the last few years.

Used in parallel and included in the VPFIT, the RDGEN program is a set of routines to handle, display and adjust data. Therefore, it is a vehicle to establish the initial values for the free parameters and also to display combined results of the VPFIT. The RDGEN and the VPFIT also require two other libraries, CFITSIO and PGPLOT. The first one is used for reading and writing data files in Flexible Image Transport System (FITS) data format. PGPLOT is a library of graphical subroutines that allows not only low-level but also high-level graph drawing.

Developed by J. Poyatos [27] and using the VPFIT and the RDGEN collection of routines, the code expects as input a FITS file with a spectrum of a QSO and also a .13 file resulting from

the quasar spectra scanning tool, QScan [28], of this same spectrum. QScan is a program that allows to scan any quasar spectrum making it easy to manually identify absorption lines.

The .13 file generated by QScan has all the information regarding the absorption systems under study. The spectrum number and the start and end wavelengths for each system, calculated by the wavelength-related redshift formula:

$$\lambda = \lambda_0(1+z), \tag{4.3}$$

where λ_0 is the wavelength of the absorption system on Earth and λ is the wavelength of the absorption system in the cloud. The file also has the Gaussian parameter and λ_0 values. In the subsequent lines, we have the first guesses/initial values (including the initial guess for the variation of α) for the fit we want, this model acts as the F^{model}. However, the atomic data file acts as F^{data}, as defined by the terminology used in equation 4.2. By trial and error, the free parameters of the model are modified so that the chi-square is improved. The redshift parameter, column density and Doppler b parameter will be modified as expected and adequate for the type of elements found in the absorption system.

As an output we will have the settings of the elements under study, as well as their associated uncertainties. The free parameters can be changed by iterations of the program itself, so that they best fit the atomic data file. We will also have the variation of α and its associated uncertainty, along with the normalized chi-square χ^2_ν. With this alpha variation determined, we have one of the key points that this dissertation covers.

For the measurement of the redshift deviation, the RDGEN program is used to generate two simulated spectra. One spectrum from the present day and one with a deviation (i.e., a simulated spectrum with the same conditions, but with an added time interval). Initially we need a .fits file of a real quasar to copy the size of the wavelength matrix. It is also necessary to take into account the wavelength dependence with noise, the Full Width at Half Maximum (FWHM) value and noise profile of the instrument, together with a .13 file with the identified absorption systems. The output is the simulated spectrum in a .fits file. For the simulation of the spectrum with an additional time interval Δt, the precision of the model parameters is only 10^{-7}, which implies that for the sensitivity of the RDGEN program a Δt of 400 years is required for a single absorption line, as demonstrated in [27]. The experiment time can be reduced by including multiple absorption lines plus those in the Lyα forest. With the two spectra obtained we can achieve the redshift drift by subtracting the two spectra or using cross-correlation. Both approaches are still the focus of discussion and are awaiting further analysis of results as in [29].

4.2 From simulated data to cosmological constraints

With the simulated spectra, as described in section 4.1, we are able to perform the astrophysical tests of fundamental physics significant to this dissertation. And we can also forecast the cosmological impact of these tests when performed by ANDES i.e., predict the uncertainties with

which to constrain the cosmological parameters with future measurements. This prediction is performed using standard Fisher Matrix analysis techniques [30][31].

A code (in Annex I) was created based on the one developed by C. S. Alves for forecasts of redshift drift constraints on cosmological parameters [11] and for forecasts for tests of the stability of the fine-structure constant [32]. Making use of Fisher Matrix techniques, our code predicts the cosmological impact of both redshift drift and the fine-structure constant measurements and also of the combination of both for several fiducial models. To better understand this code, we will define the Fisher Matrix as

$$F_{ij} = \sum_{a=1}^{N} \frac{\partial f_a}{\partial p_i} \frac{1}{{\sigma_a}^2} \frac{\partial f_a}{\partial p_j}, \tag{4.4}$$

assuming a set of parameters $(p_1, p_2, ..., p_M)$ of the model M with N observables and with $(f_1, f_2, ...f_N)$ measured quantities (i.e., predictions of the model for the N observables) with associated uncertainties $(\sigma_1, \sigma_2, ..., \sigma_N)$.

As a simple illustration, we assume a Fisher Matrix for a model with two parameters, x and y. The inverse of the calculated Fisher Matrix, the covariance matrix, gives an estimate of the covariance of the parameters given by

$$[F]^{-1} \equiv [C] = \begin{bmatrix} {\sigma_x}^2 & {\sigma_{xy}}^2 \\ {\sigma_{xy}}^2 & {\sigma_y}^2 \end{bmatrix}, \tag{4.5}$$

where ${\sigma_{xy}}^2 = \rho\sigma_x\sigma_y$ with ρ the correlation coefficient (ρ varies from -1 - independent - to $+1$ - completely correlated). The ${\sigma_x}^2$ and ${\sigma_y}^2$ are the uncertainties in parameters x and y marginalizing over the other parameters. Marginalizing a parameter in the covariance matrix simply means eliminating the column and row that are associated to it.

The covariance matrix is also a tool for drawing confidence ellipses, such as the illustrated in figure 4.1.

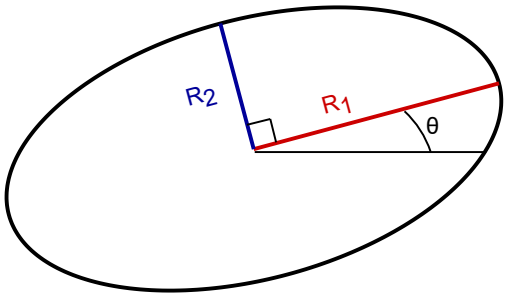

Figure 4.1: Example of a confidence ellipse.

The parameters required for drawing an ellipse like the one in figure 4.1 and following its notations are the radius of the major axis (R_1), the radius of the minor axis (R_2) defined as

$$\begin{aligned} R_1 &= \frac{\sigma_x^2 + \sigma_y^2}{2} + \sqrt{\left(\frac{\sigma_x^2 - \sigma_y^2}{2}\right)^2 + \sigma_{xy}^2} \\ R_2 &= \frac{\sigma_x^2 + \sigma_y^2}{2} - \sqrt{\left(\frac{\sigma_x^2 - \sigma_y^2}{2}\right)^2 + \sigma_{xy}^2} \end{aligned} \tag{4.6}$$

The values obtained for both radius of the ellipse are then multiplied by the coefficient associated with the confidence level we are interested in. The angle in radians from positive x-axis to the ellipse's major axis in the counterclockwise direction (θ) is given by

$$\theta = \begin{cases} 0 & \text{if } \sigma_{xy}^2 = 0 \text{ and } \sigma_x^2 \geq \sigma_y^2 \\ \frac{\pi}{2} & \text{if } \sigma_{xy}^2 = 0 \text{ and } \sigma_x^2 < \sigma_y^2 \\ atan2(R_1 - \sigma_x^2, \sigma_{xy}^2) & \text{else} \end{cases} \tag{4.7}$$

Besides the confidence ellipses we can also characterize the Figure of Merit (FoM) as

$$FoM = \frac{1}{\sigma_x \sigma_y \sqrt{1-\rho^2}(\Delta\chi^2)} = \frac{1}{({\sigma_x}^2 {\sigma_y}^2 - {\sigma_{xy}}^4)^{1/2}(\Delta\chi^2)}, \tag{4.8}$$

where $\Delta\chi^2$ classifies the confidence interval of interest. The FoM is of extreme importance due to its inverse proportionality with the confidence area of the two parameters of our model, since with a small area we have a small uncertainty in the parameters.

To summarize, the developed code will need as inputs the redshift measurements, in this case simulated data for ANDES, and the respective uncertainties of these measurements, the model and the priors we want to consider. Then it will generate the aforementioned elements, the Fisher Matrix, the covariance matrix and the FoM, from which we will be able to extract the confidence intervals and draw the confidence ellipses.

CHAPTER

5 Forecasts of Redshift Drift Measurements

Important for fundamental cosmology, redshift drift measurements are a different probe of the universe. These allow us to see the universe expanding in real time and are independent of the model considered. However, these measurements have an associated practical difficulty concerning the order of magnitude of the time scales required. The order of magnitude of cosmologically significant time scales is even larger than human time scales, which increases the difficulty related to the substantial sensitivity required in redshift drift measurements. With the telescopes available to date, the best sensitivity achieved is approximately three orders of magnitude above the expected signal for the ΛCDM model with its parameters reasonably chosen. Achieved by Darling in 2012 [33], the sensitivity is likely to be vulnerable to systematic errors on the same order of magnitude as statistical ones. Recently, Cooke also achieved a sensitivity roughly three orders of magnitude higher than the expected signal in [34].

In the detailed feasibility study of high redshift measurements for ELT with a timescale of a decade, which was performed by Liske et al. [8], they discovered that the spectroscopic velocity uncertainty is well approximated by the following expression:

$$\sigma_v = 1.35 \left(\frac{S/N}{2370}\right)^{-1} \left(\frac{N_{QSO}}{30}\right)^{-1/2} \left(\frac{1+z_{QSO}}{5}\right)^{-\lambda} \text{cm/s}, \tag{5.1}$$

where $\lambda = 1.7$ up to $z = 4$ and $\lambda = 0.9$ for $z > 4$, S/N is the signal to noise ratio, N_{QSO} the number of QSOs and z_{QSO} the effective redshift of the QSO. It should be noted that expression 5.1 was obtained based on the quasars available at that time. Consistent with this work and with the higher-level requirements for the ANDES spectrograph mentioned in [21], for an analysis of the forecasts for redshift drift we assumed a set of five effective redshifts $z_{Liske} = [2.0, 2.5, 3.0, 3.5, 4.5]$, each with $S/N = 3000$ and $N_{QSO} = 6$, a time span of $\Delta t = 20$ years and the spectroscopic velocity uncertainty is given by equation 5.1. These redshift measurements are dependent on a reasonable amount of sufficiently bright QSOs which would translate into a reasonable signal to noise when compared to telescope time. This is a plausible scenario given that the Southern hemisphere of the sky is not fully explored and searches

for additional QSOs are ongoing. With the rise in the number of available QSOs, the redshift drift measurement will increasingly tend to be a viable observational program and will take less time between the two observing epochs.

Recently, Boutsia et al. [35] proposed a new QSO catalog (still under research), the Golden Sample, with 30 bright QSOs from the Southern hemisphere at high redshift. In table 5.1 we find the names, redshift, and estimated telescope time, t in hours, for each of the QSOs. All measurements have a velocity accuracy of $\sigma_v = 22.8$ cm/s and a time span of $\Delta t = 25$ years.

Table 5.1: The Golden Sample of Southern QSO for the Sandage Test. Adapted from [35].

Name	**Redshift**	**t(h)**
J000322.94-260317.9	4.111	61.2
J000736.55-570151.8	4.260	70.5
J004131.41-493611.7	3.240	68.5
J010318.05-130509.9	4.072	71.9
J015558.26-192848.8	3.655	96.7
J015644.67-692216.1	2.800	78.7
J020413.26-325122.8	3.835	66.2
J030722.89-494548.2	4.728	78.8
J033015.31-543021.1	3.400	97.4
J042214.78-384452.9	3.123	84.2
J054803.19-484813.1	4.147	51.4
J093542.69-065118.8	4.040	85.3
J094253.51-110425.9	3.093	87.0
J101529.36-121314.3	4.190	72.0
J104856.82-163709.2	3.370	98.0
J105122.70-065047.8	3.765	88.1
J105449.68-171107.3	3.765	70.8
J111054.67-301129.8	4.780	74.2
J132029.98-052335.1	3.700	99.4
J144943.17-122717.5	3.273	82.3
J150527.83-204534.9	3.090	91.3
J162116.92-004250.8	3.703	94.1
J195302.67-381548.3	3.712	87.0
J200324.11-325145.0	3.783	83.6
J201741.49-281630.0	3.685	95.0
J212518.38-420547.6	3.549	98.8
J212540.96-171951.3	3.897	39.9
J212912.18-153840.9	3.280	88.4
J215228.21-444603.9	3.473	94.8
J215728.21-360215.1	4.771	75.7

The Golden Sample is a result of the spectroscopic follow-up of the QUasars as BRIght beacons for Cosmology in the Southern hemisphere (QUBRICS) survey. Explained in detail in [36], the QUBRICS survey is based on a canonical correlation analysis method [37] that uses several datasets such as Skymapper [38] or Gaia DR2 [39]. By employing machine learning with this photometric catalogs and the spectroscopic follow up it was possible to increase the

number of QSOs at high redshift from the southern hemisphere. Boutsia et al. selected the 30 brightest quasars, naming them the Golden Sample.

A different approach, pointed out by Klöckner et al. [40], is to use the SKAO radio telescope for low redshift measurements. This telescope is still in phase 1 of construction and only in phase 2 can redshift measurements be made with realistic time intervals between epochs. Following this approach, we assume five measurements at $z_{\mathrm{SKAO}} = 0.1, 0.2, 0.3, 0.4, 0.5$ with the uncertainties σ_{v} of $2, 4, 6, 8, 10\%$ cm/s, respectively and a time span of $\Delta t = 0.5$ years.

In order to discuss the cosmological impact of redshift measurements by the two ELT observational strategies, on their own and in combination, the Fisher Matrix techniques were used for the comparative study, as explained in section 4.2. We used two fiducial models, the well-known CPL parametrization [14][15] and one of its particular cases, the canonical ΛCDM, both discussed in section 2.1 and assuming flatness, i.e, $\Omega_{\mathrm{m}} + \Omega_{\Lambda} = 1$.

The validation of all the code, in Annex I, inherent in this chapter 5 was done behind the replication of the analysis of the fisher matrices in [11]. Achieving the same results makes it possible to use different datasets, such as the Golden Sample.

5.1 ΛCDM model

For this fiducial model the relevant cosmological parameters are $h = 0.7$, $\Omega_{\mathrm{m}} = 0.3$, $w_0 = -1$ and $w_{\mathrm{a}} = 0$ and three different cases were studied: without adding priors, with separate priors in h and Ω_{m} and with Planck prior [41] on the product of the two.

5.1.1 Without priors

The results of the analysis without priors are summarized in table 5.2 (which contains the correlation coefficients ρ of the parameters under analysis, the FoM of the pair, and one-sigma marginalized constraints for each of the model parameters) and in the left panel of figure 5.1.

From the one-sigma constraints plotted in the left panel of figure 5.1 it can be seen that the Liske dataset is reasonably competitive for Ω_{m} measurements, but its sensitivity to h is very low. This results in a relatively small FoM in the $\Omega_{\mathrm{m}} - h$ plane. On the other hand, and by the measurements summarized in table 5.2, the SKAO dataset is much more sensitive to h and thus leads to a FoM about 10 times higher than Liske. The Golden Sample dataset on its own has the least sensitivity to both parameters, yielding the smallest FoM in the $\Omega_{\mathrm{m}} - h$ plane, about 10 times smaller than Liske's. When combining Liske and SKAO datasets, we can observe that the combination, as expected, results in better one-sigma constraints, $\sigma(h) = 0.029$, for the Hubble parameter and $\sigma(\Omega_{\mathrm{m}}) = 0.012$ for the matter density and a value of FoM about 36 times higher than that of Liske on its own and almost 4 times higher than that of SKAO. The combination of Golden Sample and SKAO also improves the one-sigma constraints $\sigma(h) = 0.024$ and $\sigma(\Omega_{\mathrm{m}}) = 0.056$ and the FoM value, the sensitivity of these measurements is roughly half of the ones obtained with the combination of Liske and SKAO.

In the right panel of figure 5.1 we can see the dependence of the FoM of the Golden Sample on its velocity accuracy, σ_v. The blue horizontal line is the FoM value of Liske just for comparison. From this comparison we can infer that it will be necessary for the velocity accuracy of the Golden Sample to be improved up to $\sigma_v = 7.48$ cm/s to have the same FoM as Liske.

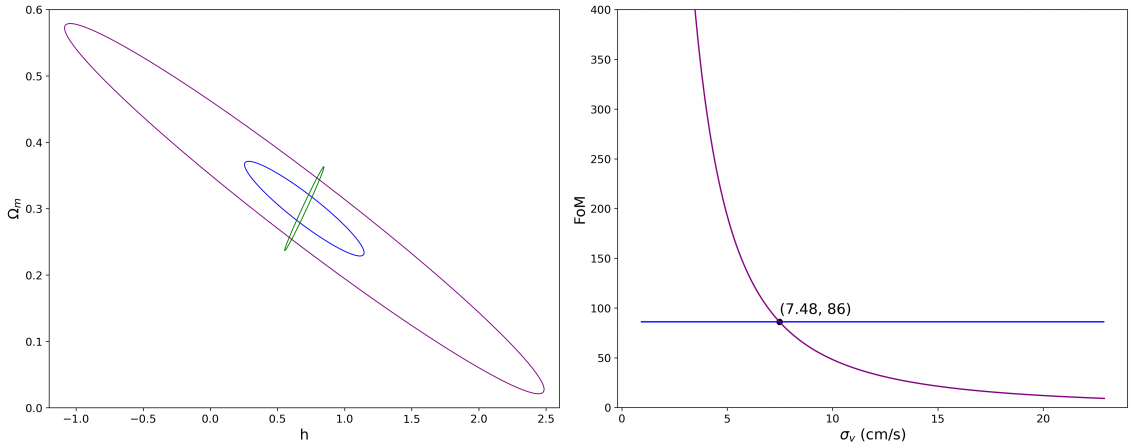

Figure 5.1: Left panel: One-sigma constraints on $\Omega_m - h$ plane. Right panel: FoM dependence on velocity accuracy of the Golden Sample dataset, compared to the FoM in the standard approach of Liske et al. (blue horizontal line). The Liske, Golden Sample and SKAO datasets are the blue, purple and green lines, respectively. Results computed using the ΛCDM model with no priors.

5.1.2 With separate priors

Separate priors were added to the parameter h and Ω_m, $\sigma_h = 0.05$ and $\sigma_{\Omega_m} = 0.03$. The results of this analysis with separate priors are also summarized in table 5.2 and in the left panel of figure 5.2.

As expected, all sensitivities were improved, such as the FoM value obtained for the $\Omega_m - h$ plane. For the Golden Sample dataset, the FoM value increases by a factor of 41, the one-sigma constraint on the h parameter improves approximately by a factor of 24, and the one-sigma constraints on the Ω_m parameter improves by a factor of 8.

In the right panel of figure 5.2 we can see the dependence of the FoM of the Golden Sample on its velocity accuracy, σ_v. The blue line is the FoM value from Liske with the addition of the separate priors just for comparison. With this comparison we can infer that to get the FoM of the Golden Sample dataset equal to the FoM of Liske the velocity accuracy will have to decrease until $\sigma_v = 9.75$ cm/s.

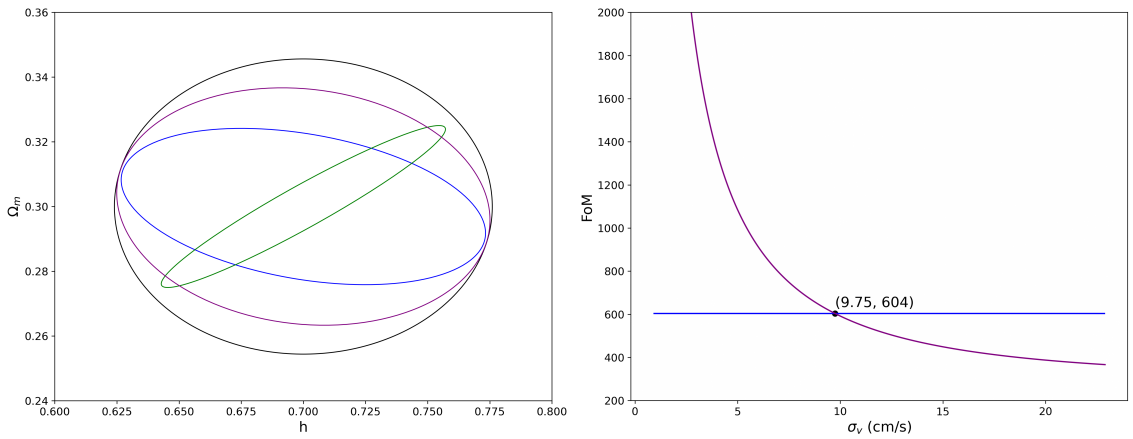

Figure 5.2: Left panel: One-sigma constraints on $\Omega_m - h$ plane. Right panel: FoM dependence on velocity accuracy of the Golden Sample dataset, compared to the FoM in the standard approach of Liske et al. (blue horizontal line). The Liske, Golden Sample and SKAO datasets are the blue, purple and green lines, respectively. The black line is the one-sigma constraint from the separate priors only. Results computed using the ΛCDM model with separate priors in h and Ω_m.

5.1.3 With Planck prior

In this analysis an external prior, the Planck Prior, was added. This prior represents the currently available data, in particular, the measurement of $\Omega_m h^2$ from the Planck 2018 [41], which has a one-sigma constraint of $\sigma_{\text{Planck}} = 0.0013$. The results of this analysis with Planck prior are also summarized in table 5.2 and in the left panel of figure 5.3.

The addition of the Planck prior leads to better constraints for the Liske and SKAO datasets. In opposition, for the Golden Sample dataset, the one-sigma constraints for the h and Ω_m parameters become worse, in particular for Ω_m, when compared to those obtained with the separate priors. The combination of datasets, either Liske+SKAO or Golden Sample+SKAO, achieve one-sigma constraints of $\sigma(h) = 0.004$ and $\sigma(\Omega_m) = 0.003$. The FoM values obtained are quite close.

In the right panel of figure 5.3 we can see the dependence of the FoM of the Golden Sample with Planck prior added on its velocity accuracy, σ_v. The blue horizontal line is the FoM value of Liske just for comparison. From this comparison we can infer that for the FoM of the Golden sample to be the same as Liske's it will require an improvement in velocity accuracy up to $\sigma_v = 9.78$ cm/s.

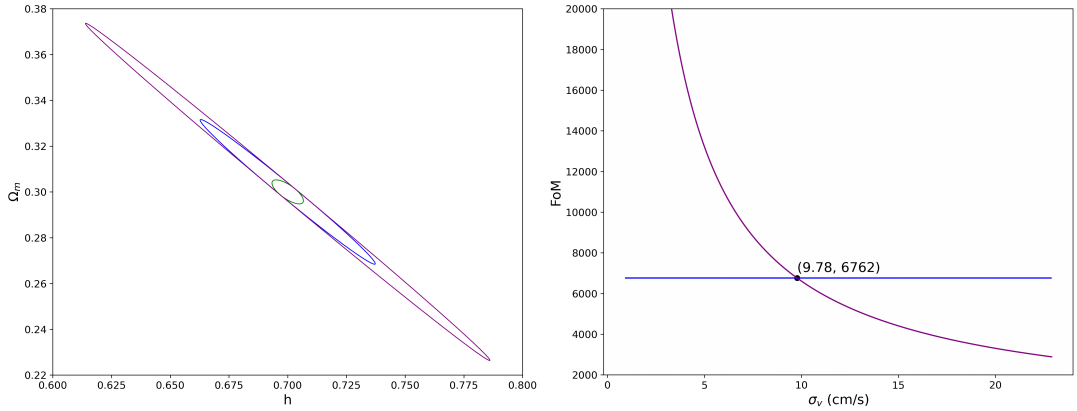

Figure 5.3: Left panel: One-sigma constraints on $\Omega_m - h$ plane. Right panel: FoM dependence on velocity accuracy of the Golden Sample dataset, compared to the FoM in the standard approach of Liske et al. (blue horizontal line). The Liske, Golden Sample and SKAO datasets are the blue, purple and green lines, respectively. Results computed using the ΛCDM model with Planck prior.

Table 5.2: Results of the Fisher Matrix analysis of redshift drift measurements for the ΛCDM model.

Datasets	**Priors**	$\rho(h, \Omega_m)$	$FoM(h, \Omega_m)$	$\sigma(h)$	$\sigma(\Omega_m)$
Liske	None	-0.930	86	0.293	0.047
	Separate	-0.340	604	0.048	0.016
	Planck	-0.992	6762	0.025	0.021
Golden Sample	None	-0.976	9	1.175	0.184
	Separate	-0.113	367	0.049	0.024
	Planck	-0.999	2900	0.057	0.048
SKAO	None	0.993	903	0.096	0.042
	Separate	0.954	2343	0.038	0.016
	Planck	-0.733	42182	0.004	0.003
Liske + SKAO	None	0.920	3081	0.029	0.012
	Separate	0.853	4422	0.021	0.009
	Planck	-0.853	60481	0.004	0.003
Golden Sample + SKAO	None	0.979	1562	0.056	0.024
	Separate	0.906	3473	0.026	0.011
	Planck	-0.855	59802	0.004	0.003

5.2 CPL parametrization

For the parametrization of the dark energy equation of state, the CPL parametrization, the fiducial cosmological parameters chosen are $h = 0.7$, $\Omega_m = 0.3$, $w_0 = -0.9$ and $w_a = 0.3$. As noted for the canonical ΛCDM in section 5.1, the results obtained with the Golden Sample dataset are comparatively worse than those obtained by the Liske and SKAO datasets. Therefore, the analysis done in the right panels of figures 5.1, 5.2 and 5.3 (i.e., the dependence of

Golden Sample's FoM on its velocity accuracy) was not performed, since with more cosmological parameters involved the FoM results would be considerably lower, as is evidenced in table 5.3. That said, for this model we analyzed through the Fisher Matrix techniques the specific case where priors were added in h, Ω_m, w_0 and w_a.

The separate priors considered were $\sigma_h = 0.05$, $\sigma_{\Omega_m} = 0.03$, $\sigma_{w_0} = 0.1$ and $\sigma_{w_a} = 0.3$. And in figure 5.4 we find two of the planes analyzed for this parametrization.

From the one-sigma constraints in the left panel it is apparent that the Liske dataset is the most competitive for Ω_m measurements, followed by the Golden Sample and soon after the SKAO. In contrast, the sensitivity of all datasets to h is qualitatively very close, making none of them stand out. In the right panel it is very clear, the best constraints obtained were those that used the SKAO dataset, regarding both w_0 and w_a. It is also noticeable, however not very pronounced, that the Like dataset is more sensitive to the w_0 parameter in contrast to the Golden Sample.

All possible planes were also analyzed, but the results obtained have the expected behavior. They were not significantly different from the planes described in detail in this section.

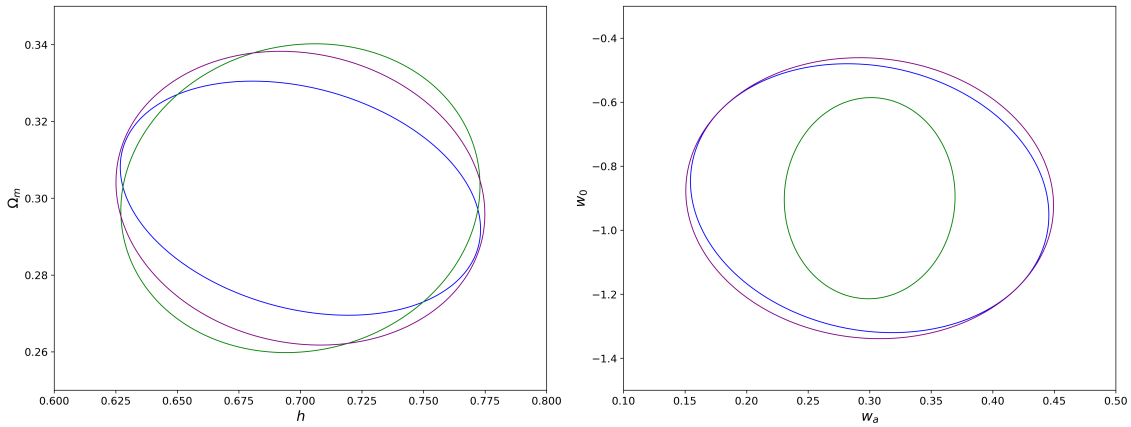

Figure 5.4: Left panel: One-sigma constraints on $\Omega_m - h$ plane. Right panel: One-sigma constraints on $w_0 - w_a$ plane. The Liske, Golden Sample and SKAO datasets are the blue, purple and green lines, respectively. Results computed using the CPL parametrization with separate priors in h, Ω_m, w_0 and w_a.

In table 5.3 we can find the correlation coefficient, ρ, and FoM of the various parameter combinations, marginalizing the others. And also the one-sigma constraint, σ, of each of the parameters is listed. Comparing the FoM measurements obtained for the parameter set (h, Ω_m) with the Separate Priors case in table 5.2, we can observe that the largest decrease in the FoM value obtained is for the SKAO, by a factor of approximately 6.8. However, for the Golden Sample dataset, the decrease in FoM is only 1.04. Regarding the one-sigma constraints, the value of $\sigma(h)$ remains unchanged for the analysis with the isolated Liske and Golden Sample datasets and for the remaining cases it increases. Meanwhile, for $\sigma(\Omega_m)$, the uncertainty increases in comparison to those presented in table 5.2 both for isolated datasets and in combinations. For the other parameter sets, we can observe that the results agree with

the predictions. Increasing the number of free parameters with respect to those in the ΛCDM model lowers the sensitivity to each of the parameters and the value of the FoM. The highest FoM value is achieved when the datasets are combined, in particular in the set (Ω_m, w_0). The lowest one-sigma constraints obtained for w_0 and w_a are $\sigma(w_0) = 0.032$ and $\sigma(w_a) = 0.164$ both for the combination of the Liske and SKAO datasets.

Table 5.3: Results of the Fisher Matrix analysis of redshift drift measurements for the CPL model.

Parameters	**Liske**	**Golden Sample**	**SKAO**	**Liske + SKAO**	**Golden Sample + SKAO**
$\boldsymbol{\rho(h, \Omega_m)}$	-0.266	-0.108	0.081	-0.163	0.024
$\boldsymbol{\rho(\Omega_m, w_0)}$	-0.286	-0.120	-0.712	-0.688	-0.700
$\boldsymbol{\rho(h, w_0)}$	-0.039	-0.030	0.558	0.702	0.570
$\boldsymbol{\rho(\Omega_m, w_a)}$	-0.436	-0.181	-0.404	-0.411	-0.317
$\boldsymbol{\rho(h, w_a)}$	-0.071	-0.045	-0.064	-0.059	-0.036
$\boldsymbol{\rho(w_0, w_a)}$	-0.125	-0.053	0.016	-0.074	-0.093
$\boldsymbol{FoM(h, \Omega_m)}$	467	353	344	902	730
$\boldsymbol{FoM(\Omega_m, w_0)}$	236	177	513	1207	1026
$\boldsymbol{FoM(h, w_0)}$	94	90	239	602	479
$\boldsymbol{FoM(\Omega_m, w_a)}$	87	61	87	187	155
$\boldsymbol{FoM(h, w_a)}$	33	31	44	84	79
$\boldsymbol{FoM(w_0, w_a)}$	17	15	46	83	80
$\boldsymbol{\sigma(h)}$	0.048	0.049	0.048	0.032	0.033
$\boldsymbol{\sigma(\Omega_m)}$	0.020	0.025	0.026	0.015	0.018
$\boldsymbol{\sigma(w_0)}$	0.096	0.098	0.046	0.032	0.033
$\boldsymbol{\sigma(w_a)}$	0.276	0.289	0.207	0.164	0.166

CHAPTER

6 Forecasts of the Stability of the Fine-Structure Constant

Used to describe the forces present in the physical interactions in the standard model of particle physics, the dimensionless fundamental couplings were assumed to be invariant in space-time. As discussed by C.J.A.P. Martins in [42], experiments in particle accelerators have shown that the behavior of fundamental couplings has a dependence on energy, and therefore, in various extensions of the standard model, these couplings will change in time and perhaps in space. High resolution spectroscopic measurements of the fine-structure constant α have particular importance in the field of astrophysical tests of the stability of fundamental couplings. In a scenario where the same dynamical degree of freedom represents alpha variation and dark energy, the obtained cosmological constraints can be combined with the standard cosmological observables and thus constrain the equation of state of dark energy, as explained in [43] and [44]. Meanwhile, in any scenario, the variation when detected will imply a violation of Einstein's Equivalence Principle, further details in [45].

In agreement with the ANDES specifications two datasets were simulated with baseline and optimistic forecasts, respectively. For the baseline hypothesis we assumed 15 redshift measurements between $z = 1.0$ and $z = 2.5$, equally spaced, and with an uncertainty $\sigma_\alpha = 0.1$ ppm and 10 redshift measurements between $z = 2.5$ and $z = 4.0$, also equally spaced, and with an uncertainty $\sigma_\alpha = 0.2$ ppm. For a more optimistic scenario, we assumed three different sets of redshift measurements. The first one with 20 redshift measurements between $z = 1.0$ and $z = 2.5$ and with an uncertainty $\sigma_\alpha = 0.05$ ppm. The second with 15 redshift measurements between $z = 2.5$ and $z = 4.0$ and with an uncertainty $\sigma_\alpha = 0.1$ ppm. The third with 15 redshift measurements between $z = 4.0$ and $z = 7.0$ and with an uncertainty $\sigma_\alpha = 1$ ppm. All redshift measurements of the sets are equally spaced.

Aiming to discuss the cosmological impact of the fine-structure constant variation measurements from the baseline and optimistic datasets, Fisher Matrix techniques were used for the comparative study, as explained in section 4.2. One type of each class of models was analyzed, the CPL parametrization [14][15] representing the Class I models and the Bekenstein-type

model [16] representing the Class II.

The validation of all the code, in Annex I, inherent in this chapter 6 was done behind the replication of the analysis of the fisher matrices in [46]. Achieving the same results makes it possible to use different datasets, such as the forecasts for ANDES.

6.1 Bekenstein-type model

For Class II models, such as the Bekenstein model used here, the relative variation of α is given by equation 2.11, as already explained in section 2.1. And it is important to remember that in this case, the flat ΛCDM is assumed and which implies $w_0 = -1$ and $w_a = 0$.

The present-day drift rate for this model is given by:

$$\left(\frac{1}{H}\frac{\dot{\alpha}}{\alpha}\right)_0 = -\zeta_\Lambda + 2(\zeta_\Lambda - 2\zeta_m)\frac{\Omega_m}{\sqrt{\Omega_\Lambda}}\log\left(\frac{1+\sqrt{\Omega_\Lambda}}{\sqrt{\Omega_m}}\right) \tag{6.1}$$

Achieved by Rosenband et al. [47], the present variation of α determined in the atomic clock laboratory assumes the value of:

$$\left(\frac{1}{H}\frac{\dot{\alpha}}{\alpha}\right)_0 = -0.22 \pm 0.32\text{ppm} \tag{6.2}$$

From equation 6.1 and the uncertainty in equation 6.2 we can determine the prior uncertainties from the atomic clocks for both ζ. The fiducial value for both is $\zeta_\Lambda = \zeta_m = -0.1\times10^{-6} = -0.1$ ppm. For Ω_m it is once again used $\Omega_m = 0.3$ and $\sigma(\Omega_m) = 0.03$.

Figure 6.1 displays the results of the analysis using the Fisher Matrix techniques for the Bekenstein model. We can observe in the left and central panels that the constraints obtained with both baseline and optimistic forecasts are equally sensitive to the Ω_m parameter. Nevertheless, the optimistic forecasts are more sensitive to both ζ_m and ζ_Λ when compared to the baseline forecasts.

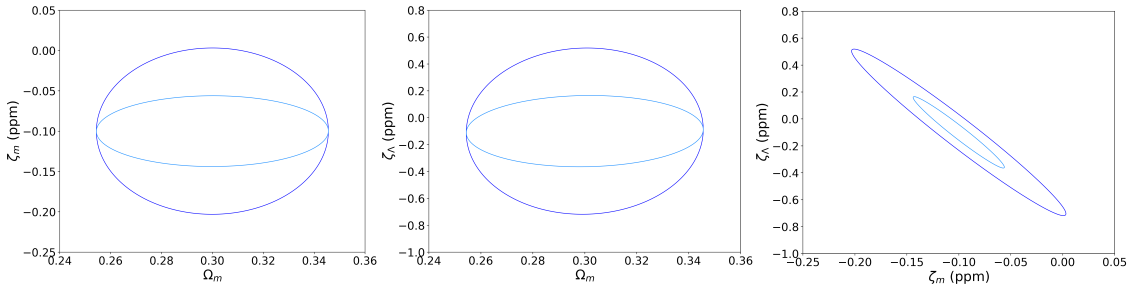

Figure 6.1: Left panel: One-sigma constraints on $\zeta_m - \Omega_m$ plane. Middle panel: One-sigma constraints on $\zeta_\Lambda - \Omega_m$ plane. Right panel: One-sigma constraints on $\zeta_\Lambda - \zeta_m$ plane. The datasets with baseline and optimistic forecasts correspond to the dark blue and light blue lines, respectively and for the Bekenstein model.

Table 6.1 shows the correlation coefficients of the various sets of model parameters, the FoM and the one-sigma constraints achieved through this analysis. The ζ_m and ζ_Λ parameters

were expressed in ppm. Compared to table 6.2, in table 6.1 it is noticeable in all the correlation coefficients and FoM that the value obtained rises when the optimistic forecasts are used. As presented in figure 6.1, both forecasts are equally sensitive to Ω_m. As for ζ_m and ζ_Λ, the optimistic forecasts are the ones that better constrain both parameters, i.e. smaller values of the one-sigma constraints. It should also be emphasized that there is no correlation between the cosmological parameter, Ω_m, and the particle physics parameters, ζ_m and ζ_Λ, of this model. It follows that the Ω_m parameter does not benefit the change from baseline to optimistic forecasts. The biggest improvement perceived is in the (ζ_m, ζ_Λ) set which, from the correlation coefficient, we can clearly see the anti-correlation between them.

Table 6.1: Results of the Fisher Matrix analysis of α variation measurements for the Bekenstein model.

Parameters	**Baseline**	**Optimistic**
$\boldsymbol{\rho(\Omega_m, \zeta_m)}$	0.002	0.005
$\boldsymbol{\rho(\Omega_m, \zeta_\Lambda)}$	0.020	0.045
$\boldsymbol{\rho(\zeta_m, \zeta_\Lambda)}$	-0.976	-0.975
$\boldsymbol{FoM(\Omega_m, \zeta_m)}$	214	502
$\boldsymbol{FoM(\Omega_m, \zeta_\Lambda)}$	36	83
$\boldsymbol{FoM(\zeta_m, \zeta_\Lambda)}$	73	391
$\boldsymbol{\sigma(\Omega_m)}$	0.030	0.030
$\boldsymbol{\sigma(\zeta_m)}$	0.068	0.029
$\boldsymbol{\sigma(\zeta_\Lambda)}$	0.407	0.174

6.2 CPL parametrization

For this parametrization the relative variation of α is given by equation 2.5 described in section 2.1. We realistically choose the subsequent fiducial values and prior uncertainties for our cosmological and particle physics parameters:

$$\Omega_m = 0.3, \sigma(\Omega_m) = 0.03$$
$$w_0 = -0.9, \sigma(w_0) = 0.1$$
$$w_a = 0.3, \sigma(w_a) = 0.3$$
$$\zeta = -0.1 \times 10^{-6} = -0.1 \text{ ppm}, \sigma(\zeta) = 10^{-5} = 10 \text{ ppm}$$

From the analysis of the one-sigma constraints of the three panels presented in figure 6.2, it is noticeable that whether with the baseline or optimistic forecasts, the sensitivity to Ω_m, w_0 and w_a is the same for the two cases. On the other hand, and as would be expected, the optimistic forecasts lead to better ζ constraints than the baseline ones.

In table 6.2 we present the correlation coefficients of the various sets of model parameters, the FoM and the one-sigma constraints obtained. The ζ parameter was expressed in ppm. The largest differences between the baseline and optimistic forecasts in the achieved FoM values are for the sets (w_0, ζ) and (w_a, ζ) where the increase factor is roughly 1.5. The others

vary by a smaller factor or do not vary approximately at all as in the case of the set (Ω_m, w_0), (Ω_m, w_a) and (w_0, w_a). These different results than expected are due to the correlation that the particle physics parameter ζ exhibits with w_0 and w_a. Leading to a decrease in the one-sigma constraint of the ζ parameter, $\sigma(\zeta)$, and a slight increase in the constraints $\sigma(w_0)$ and $\sigma(w_a)$. This increase and decrease in the one-sigma constraints is a result in agreement with that obtained by Calabrese et al. in [48]. Regarding one-sigma constraints for the parameters w_0 and w_a, optimistic forecasts only improve the uncertainty of w_a. For the ζ parameter, it is noticeable that the optimistic forecasts lead to a smaller one-sigma constraint value.

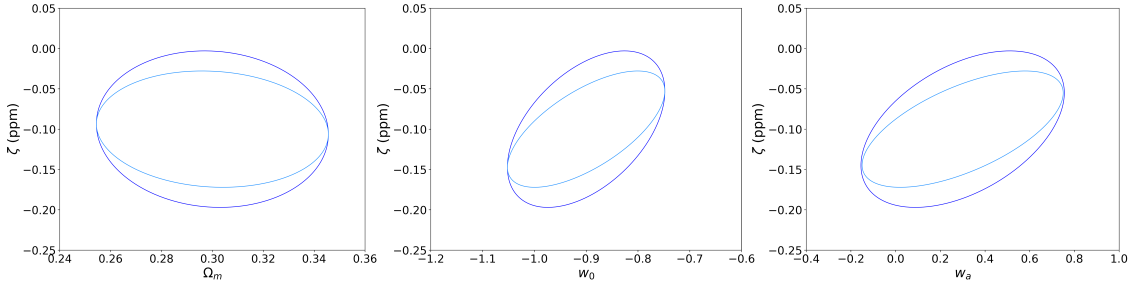

Figure 6.2: Left panel: One-sigma constraints on $\zeta - \Omega_m$ plane. Middle panel: One-sigma constraints on $\zeta - w_0$ plane. Right panel: One-sigma constraints on $\zeta - w_a$ plane. The datasets with baseline and optimistic forecasts correspond to the dark blue and light blue lines, respectively and for the CPL parametrization.

Table 6.2: Results of the Fisher Matrix analysis of α variation measurements for the CPL parametrization.

Parameters	**Baseline**	**Optimistic**
$\boldsymbol{\rho(\Omega_m, w_0)}$	-0.000	-0.000
$\boldsymbol{\rho(\Omega_m, w_a)}$	0.000	0.002
$\boldsymbol{\rho(\Omega_m, \zeta)}$	-0.067	-0.089
$\boldsymbol{\rho(w_0, w_a)}$	0.000	0.000
$\boldsymbol{\rho(w_0, \zeta)}$	0.486	0.654
$\boldsymbol{\rho(w_a, \zeta)}$	0.464	0.620
$\boldsymbol{FoM(\Omega_m, w_0)}$	145	145
$\boldsymbol{FoM(\Omega_m, w_a)}$	48	49
$\boldsymbol{FoM(\Omega_m, \zeta)}$	228	307
$\boldsymbol{FoM(w_0, w_a)}$	15	15
$\boldsymbol{FoM(w_0, \zeta)}$	78	121
$\boldsymbol{FoM(w_a, \zeta)}$	26	39
$\boldsymbol{\sigma(\Omega_m)}$	0.030	0.030
$\boldsymbol{\sigma(w_0)}$	0.100	0.100
$\boldsymbol{\sigma(w_a)}$	0.299	0.296
$\boldsymbol{\sigma(\zeta)}$	0.064	0.047

CHAPTER

7 Forecasts of Combined Redshift Drift and Fine-Structure Constant Measurements

After the separate analysis of forecasts of both redshift drift measurements and the stability of the fine-structure constant in chapters 5 and 6 respectively, it is now important to analyze the combination of redshift drift and α measurements and what gains come from this combination.

To analyze the gain, we have made two combinations of datasets, both including redshift drift and α measurements. First, we combined the Liske dataset, described in chapter 5, with the baseline forecast, discussed in chapter 6. The second combination is again the Liske dataset, but combined with the optimistic forecast, also described in chapter 6. The Fisher Matrix analysis for the combination of the redshift drift and α measurements simply results from adding the matrices obtained separately. These analyses were carried out for the Bekenstein model and the CPL parametrization and using the same realistic choices for both the fiducial values and the prior uncertainties.

Subsequently, we further quantified the constraints on the model parameters from the combined data by drawing the likelihoods of each parameter. For this quantification, two cases were chosen for the CPL parametrization, $w_0 = -1$ and $w_a = 0$ (the ΛCDM particular case already described in subsection 2.1) and $w_0 = -0.9$ and $w_a = 0.3$, the CPL case used in the previous analyses. And also two distinct cases for the Bekenstein model, the first where $\zeta_m = \zeta_\Lambda = 0$ (i.e. the ΛCDM model is recovered) and the other where $\zeta_m = \zeta_\Lambda = -0.1$ ppm.

7.1 Bekenstein-type model

In figure 7.1 are presented the most relevant 2D planes of the one-sigma constraints for the Bekenstein model and using the baseline α forecasts. In the upper right panel, the only panel in which the three constraints at one-sigma are represented, we can deduce that the gain from the combination of redshift drift and alpha measurements is extremely small. In particular, the constraints obtained for h and Ω_m are coincident and therefore the three ellipses are overlapping. In the remaining panels involving the ζ_m and ζ_Λ parameters we realize that the

combination of the measurements (dark purple lines) has a larger gain for the $\Omega_{\rm m}$ parameter, as for the CPL parametrization.

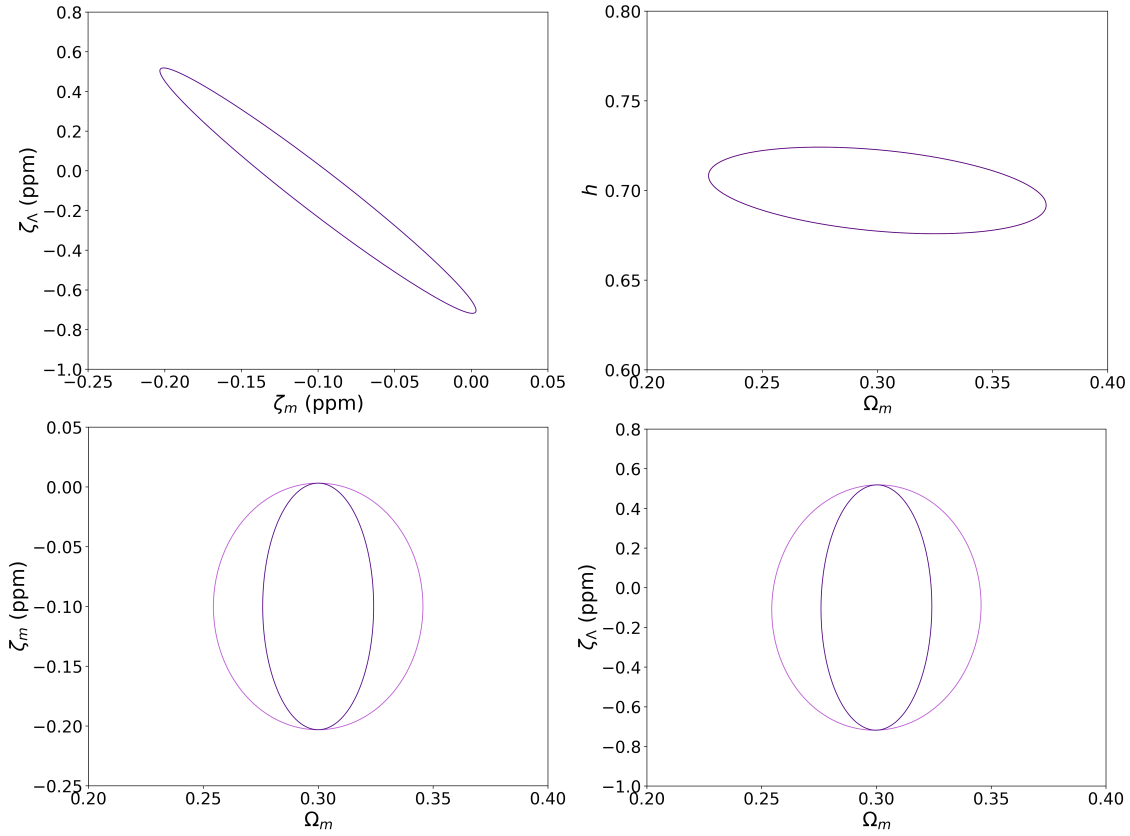

Figure 7.1: One-sigma constraints for the most relevant combinations of the Bekenstein model parameters (h, $\Omega_{\rm m}$, $\zeta_{\rm m}$ and ζ_Λ). The Liske dataset with redshift drift measurements only, the baseline forecasts with α measurements only, and the combination of redshift drift and α correspond to the red, light purple, and dark purple lines, respectively. The red line drawn only in the upper right panel is not visible, as it is superimposed on the dark purple line.

In figure 7.2 we have used the optimistic forecasts for α measurements and all ellipses behave as expected, that is, tighter constraints on $\Omega_{\rm m}$, $\zeta_{\rm m}$ and ζ_Λ.

Table 7.1 summarizes the FoM values of all the parameter sets and the one-sigma constraints of each of them from the Fisher Matrix analysis of the entire datasets for the Bekenstein model.

We can infer from figures 7.1 and 7.2 and table 7.1 that redshift drift constrains the cosmological parameters, α variation constraints the couplings and the combination improves the constraint on $\Omega_{\rm m}$.

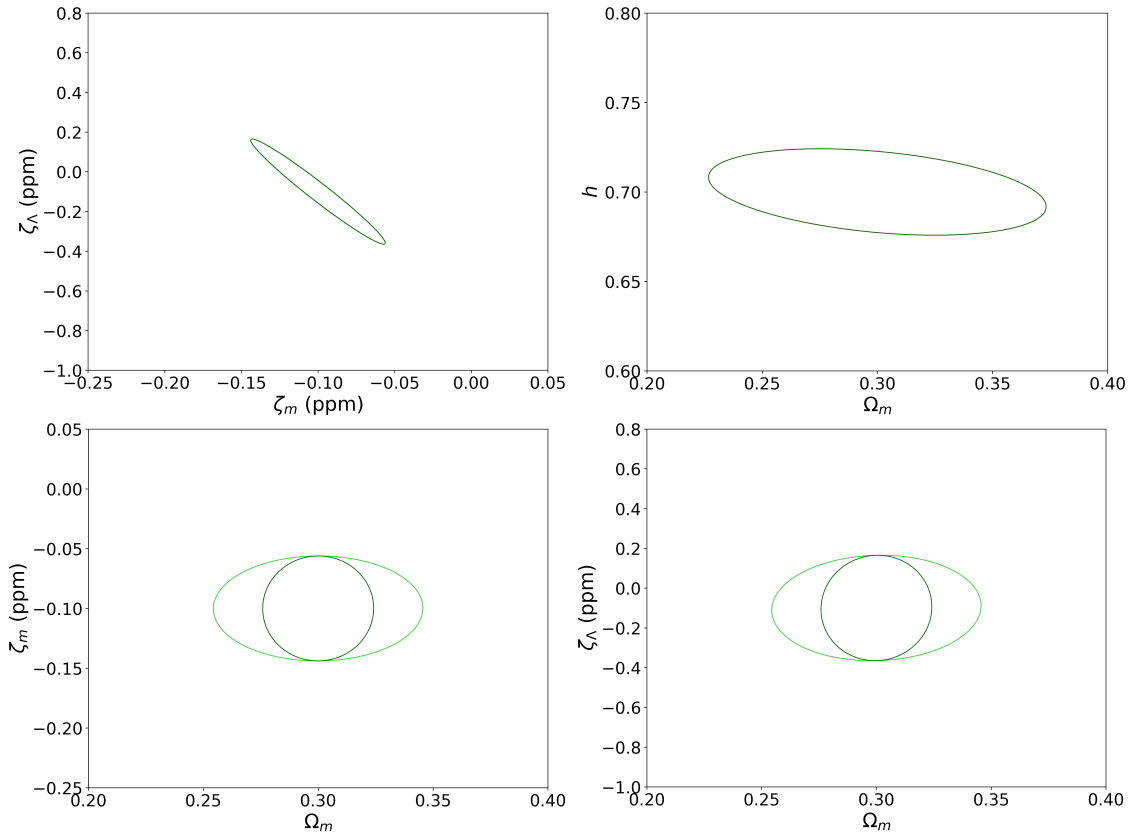

Figure 7.2: One-sigma constraints for the most relevant combinations of the Bekenstein model parameters (h, Ω_m, ζ_m and ζ_Λ). The Liske dataset with redshift drift measurements only, the optimistic forecasts with α measurements only, and the combination of redshift drift and α correspond to the red, light green, and dark green lines, respectively. The red line drawn only in the upper right panel is not visible, as it is superimposed on the dark green line.

Table 7.1: Results of the Fisher Matrix analysis of redshift drift, α and combination of both measurements for the Bekenstein model.

Parameters	**Liske**	**Baseline**	**Optimistic**	**Liske + Baseline**	**Liske + Optimistic**
$\boldsymbol{FoM(\zeta_\mathrm{m}, \zeta_\Lambda)}$	-	73	391	73	399
$\boldsymbol{FoM(\zeta_\mathrm{m}, \Omega_\mathrm{m})}$	-	214	502	403	948
$\boldsymbol{FoM(\zeta_\Lambda, \Omega_\mathrm{m})}$	-	36	83	67	157
$\boldsymbol{FoM(\Omega_\mathrm{m}, h)}$	604	-	-	604	604
$\boldsymbol{\sigma(h)}$	0.048	-	-	0.048	0.048
$\boldsymbol{\sigma(\Omega_\mathrm{m})}$	0.016	0.030	0.030	0.016	0.016
$\boldsymbol{\sigma(\zeta_\mathrm{m})}$	-	0.068	0.029	0.068	0.029
$\boldsymbol{\sigma(\zeta_\Lambda)}$	-	0.407	0.174	0.407	0.174

Figure 7.3 displays the 1D posterior likelihoods obtained for each of the parameters of the Bekenstein models. It can be observed that there is no visible distinction of the models $\zeta_\mathrm{m} = \zeta_\Lambda = 0$ and $\zeta_\mathrm{m} = \zeta_\Lambda = -0.1$ ppm for the h and Ω_m parameters, which is not unexpected since the fiducial values are the same. However, the major distinction of the two models

is when we analyze the likelihoods obtained for the $\zeta_{\rm m}$ parameter, in particular using the optimistic forecasts of the α measurements.

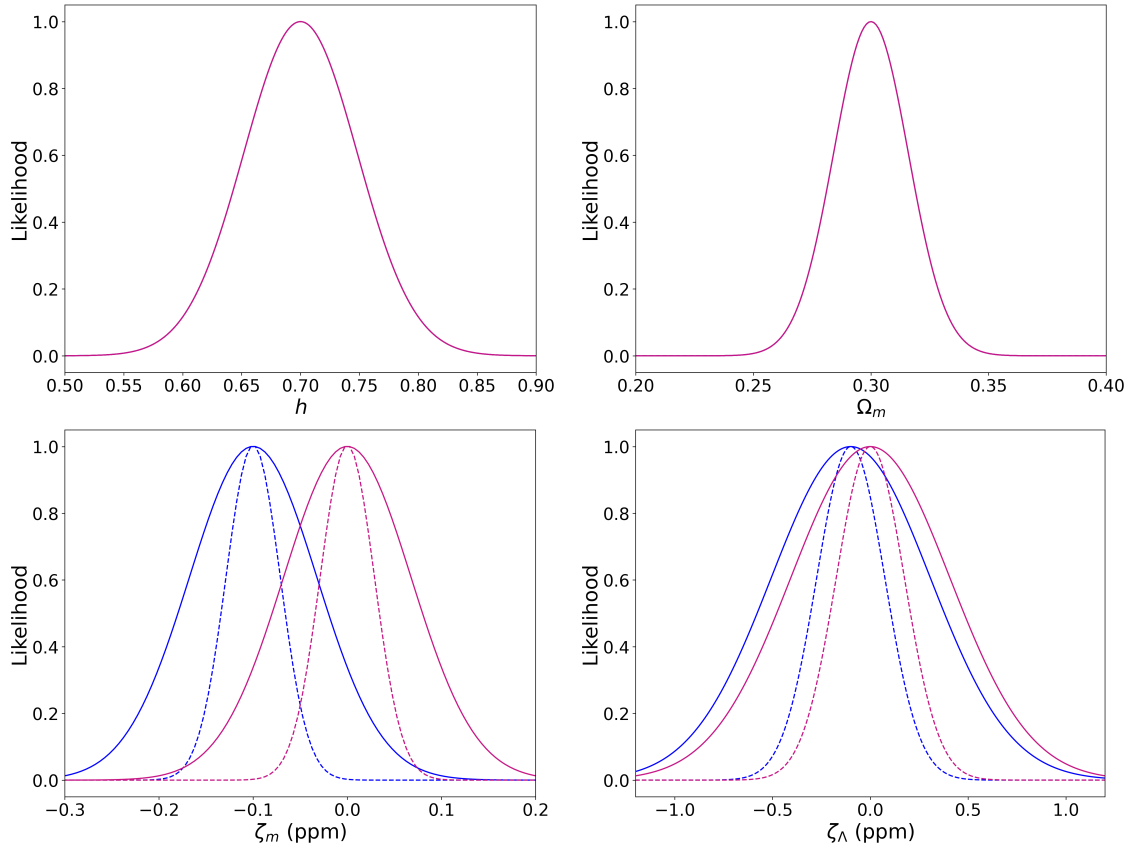

Figure 7.3: One-dimensional likelihood for each parameter of the Bekenstein model. The combinations of the Liske dataset with baseline and optimistic forecasts are the solid and dashed lines, respectively. Concerning the models, $\zeta_{\rm m} = \zeta_\Lambda = -0.1$ ppm it is represented in the blue lines and $\zeta_{\rm m} = \zeta_\Lambda = 0$ it is in the pink ones.

7.2 CPL parametrization

Figure 7.4 shows the most relevant 2D planes of the one-sigma constraints for the CPL parametrization and using the baseline α forecasts. In the top three panels, the $\zeta - w_{\rm a}$, $\zeta - w_0$ and $\zeta - \Omega_{\rm m}$ planes, we have the one-sigma constraints for α only measurements and the combination of these with redshift drift. From the analysis of these three panels, it is clear that the biggest gain is seen in the one where the $\Omega_{\rm m}$ parameter is involved. That is, in the $\zeta - \Omega_{\rm m}$ panel, the one-sigma constraints in dark purple (combination of alpha and redshift drift measurements) significantly improve the sensitivity to $\Omega_{\rm m}$. The reason for this difference is that redshift drift does not depend directly on ζ, but is highly sensitive to $\Omega_{\rm m}$. The central three panels show the one-sigma constraints for measurements of redshift drift only, α only, and combination of the two. For these three cases the gains from the combination of redshift drift and α measurements are not easily distinguishable, since they are presented overlapped with the one-sigma

constraints from redshift drift measurements only i.e., the red and dark purple lines are overlapping. It should be noted that the $w_a - w_0$ panel is where we have the smallest gain that comes from combining the measurements. Finally, in the bottom three panels where one of the parameters is h, the one-sigma constraints of redshift drift measurements and of the combination of redshift drift with α are plotted. For both the w_0 and Ω_m parameters the improvement is not visible, as the red lines (from redshift drift only) are superimposed on the dark purple lines (from the combination of redshift drift and α). In contrast, in the $w_a - h$ panel we can see the increased sensitivity to the w_a parameter when we combine the measurements.

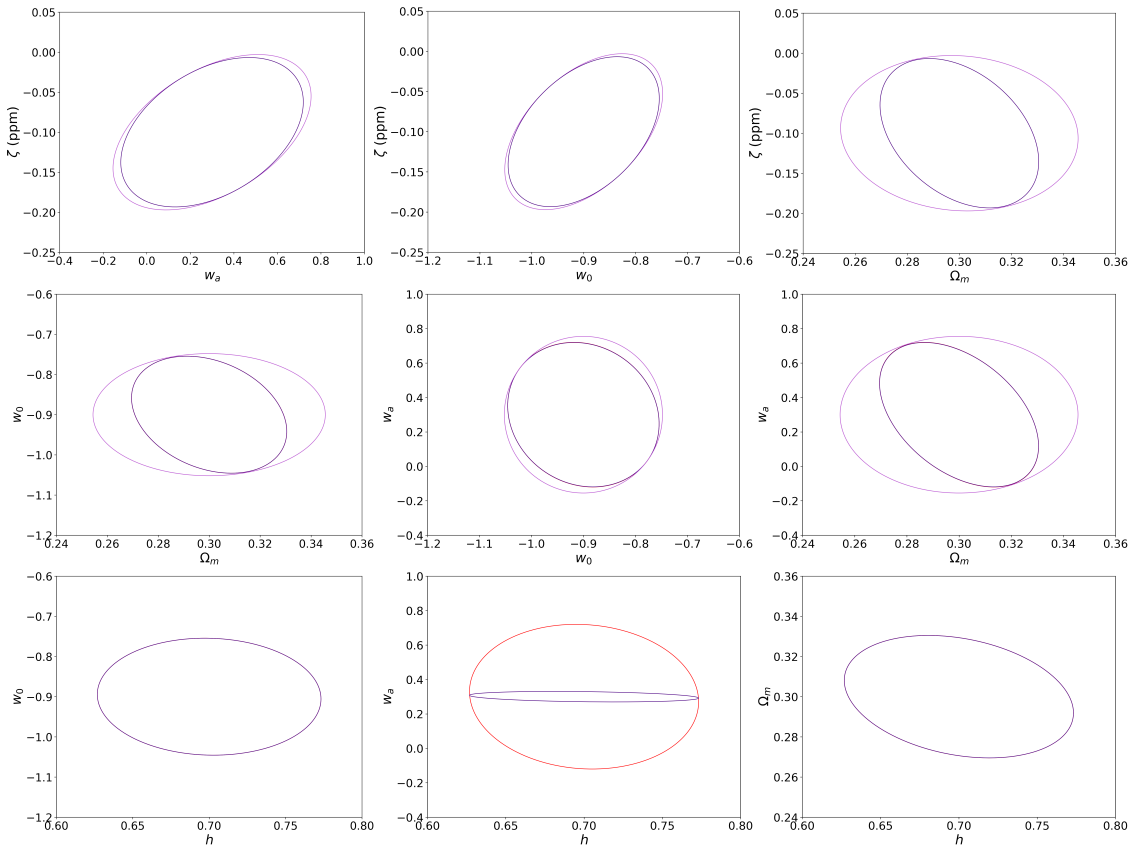

Figure 7.4: One-sigma constraints for the most relevant combinations of the CPL parametrization parameters (h, Ω_m, w_0, w_a and ζ). The Liske dataset with redshift drift measurements only, the baseline forecasts with α measurements only, and the combination of redshift drift and α correspond to the red, light purple, and dark purple lines, respectively. The red lines drawn in the middle and bottom panels when not visible are superimposed on the dark purple lines.

The same parameter combinations as in figure 7.4 are plotted in figure 7.5 however, using optimistic α forecasts. By directly comparing both results, with baseline and optimistic forecasts, we can verify that the results of the optimistic forecasts follow what is expected for this type of forecast. It is easy to notice that in the central panels the gain relative to the combination of the two types of measurements, however with a very small difference, is already detectable in the plots i.e., we can see the one-sigma constraints of redshift drift measurements

(red lines), α measurements (light green lines) and the combination of both (dark green lines).

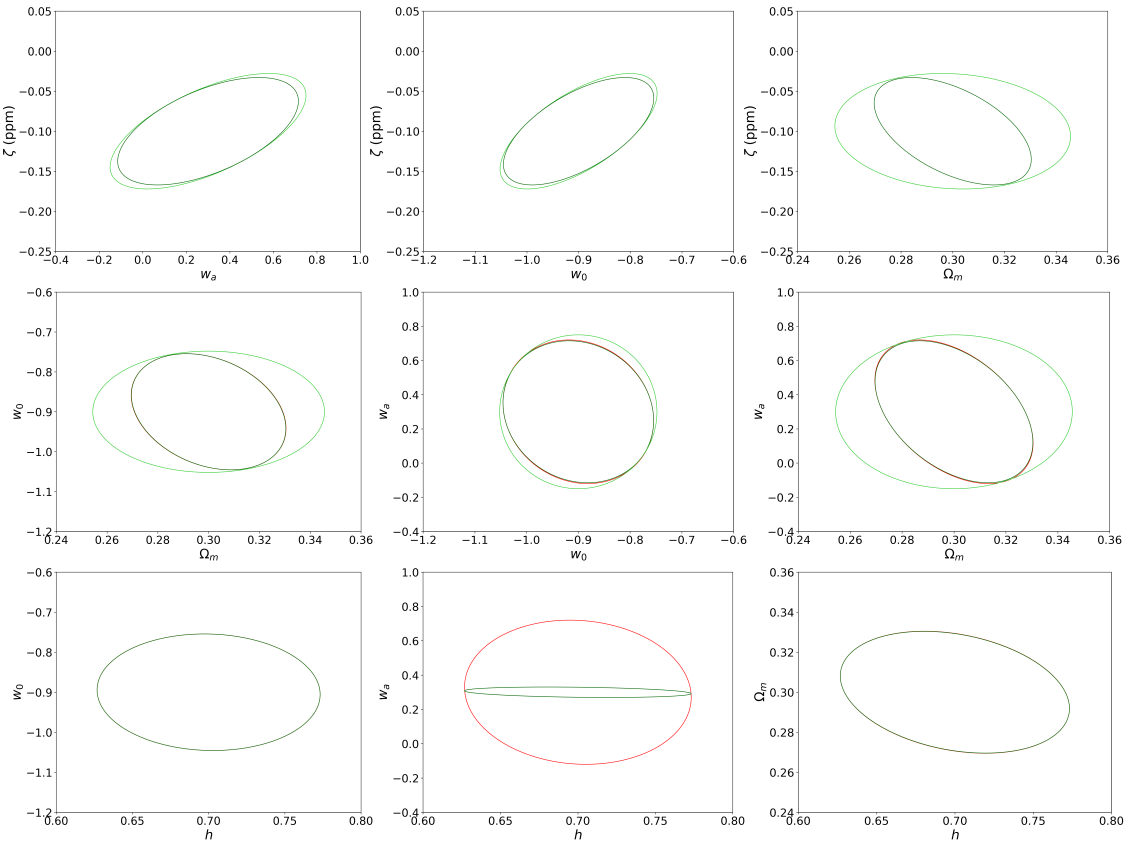

Figure 7.5: One-sigma constraints for the most relevant combinations of the CPL parametrization parameters (h, $\Omega_{\rm m}$, w_0, $w_{\rm a}$ and ζ). The Liske dataset with redshift drift measurements only, the optimistic forecasts with α measurements only, and the combination of redshift drift and α correspond to the red, light green, and dark green lines, respectively. The red lines drawn in the middle and bottom panels when not visible are superimposed on the dark green lines.

Table 7.2 presents the FoM of all possible sets of parameters of the CPL parametrization, marginalizing the remaining ones, and the one-sigma constraints obtained for each parameter individually. We can observe that for the combinations that include ζ, the $\zeta - \Omega_{\rm m}$ combination is where we obtain the largest gain when combining redshift drift and alpha measurements, in particular with optimistic α forecasts. For the combinations $w_{\rm a} - \Omega_{\rm m}$, $w_0 - \Omega_{\rm m}$ we can remark that the FoM is mostly determined by the constraints obtained for the Liske dataset. And the lower FoM values for optimistic forecasts than for baseline are due to the change in the degeneracy direction of the obtained ellipses. We also confirm that for the $w_{\rm a} - w_0$ panel the differences between the combined and individually acquired FoM values are not significant. Regarding one-sigma constraints it is clearly seen that the combination of the measurements does not imply better constraints on the parameters than those obtained with the Liske dataset. The exception is the ζ parameter where combining Liske and optimistic α forecasts the obtained value is $\sigma(\zeta) = 0.044$.

Table 7.2: Results of the Fisher Matrix analysis of redshift drift, α and combination of both measurements for the CPL parametrization.

Parameters	**Liske**	**Baseline**	**Optimistic**	**Liske + Baseline**	**Liske + Optimistic**
$\boldsymbol{FoM(\zeta, w_a)}$	-	26	39	28	44
$\boldsymbol{FoM(\zeta, w_0)}$	-	78	121	82	131
$\boldsymbol{FoM(\zeta, \Omega_m)}$	-	228	307	382	579
$\boldsymbol{FoM(w_a, w_0)}$	17	15	15	17	17
$\boldsymbol{FoM(w_a, \Omega_m)}$	87	48	49	87	88
$\boldsymbol{FoM(w_0, \Omega_m)}$	236	145	145	236	237
$\boldsymbol{FoM(w_a, h)}$	33	-	-	33	33
$\boldsymbol{FoM(w_0, h)}$	94	-	-	94	94
$\boldsymbol{FoM(\Omega_m, h)}$	467	-	-	467	469
$\boldsymbol{\sigma(h)}$	0.048	-	-	0.048	0.048
$\boldsymbol{\sigma(\Omega_m)}$	0.020	0.030	0.030	0.020	0.020
$\boldsymbol{\sigma(w_0)}$	0.096	0.100	0.100	0.096	0.096
$\boldsymbol{\sigma(w_a)}$	0.276	0.299	0.296	0.276	0.273
$\boldsymbol{\sigma(\zeta)}$	-	0.064	0.047	0.061	0.044

Figure 7.6 shows the likelihoods obtained for each of the parameters of the CPL parametrization, in the green lines we find the case $w_0 = -0.9$ and $w_a = 0.3$, while the orange lines represent the case $w_0 = -1$ and $w_a = 0$. For these models the distinction between them is most noticeable for the ζ parameter and imperceptible for h. For the parameters w_0 and w_a the likelihoods are centered on the respective most likely values, but the difference between each model is very similar compared to each other.

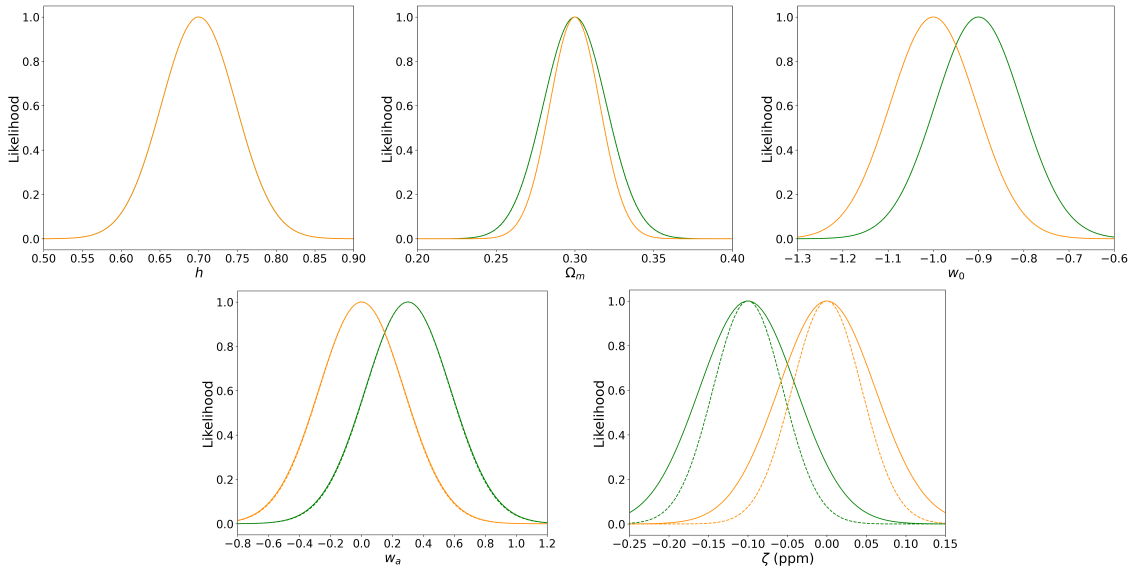

Figure 7.6: One-dimensional likelihood for each parameter of the CPL parametrization. The combinations of the Liske dataset with baseline and optimistic forecasts are the solid and dashed lines, respectively. Concerning the models, $w_0 = -0.9$ and $w_a = 0.3$ it is represented in the green lines and $w_0 = -1$ and $w_a = 0$ it is in the orange ones.

7.3 Comparison between ΛCDM, Bekenstein and CPL parametrization

In figure 7.7 we represent the 1D posterior likelihoods for the parameters w_0, w_a, ζ, ζ_m and ζ_Λ without any model class assumed, i.e., without knowing beforehand whether the degree of freedom accounts for the variable constants as for the dark energy or whether, on the contrary, the field that provides the variable couplings does not provide the dark energy. This leads us to conclude that without additional class information it is not possible, with the type of analysis of the Fisher Matrices, to identify the type of model that best fits the data.

The panels that are not represented (the h and Ω_m parameters) were purposely not included because the three likelihoods are overlapping. An expected result considering that the fiducial values used are the same.

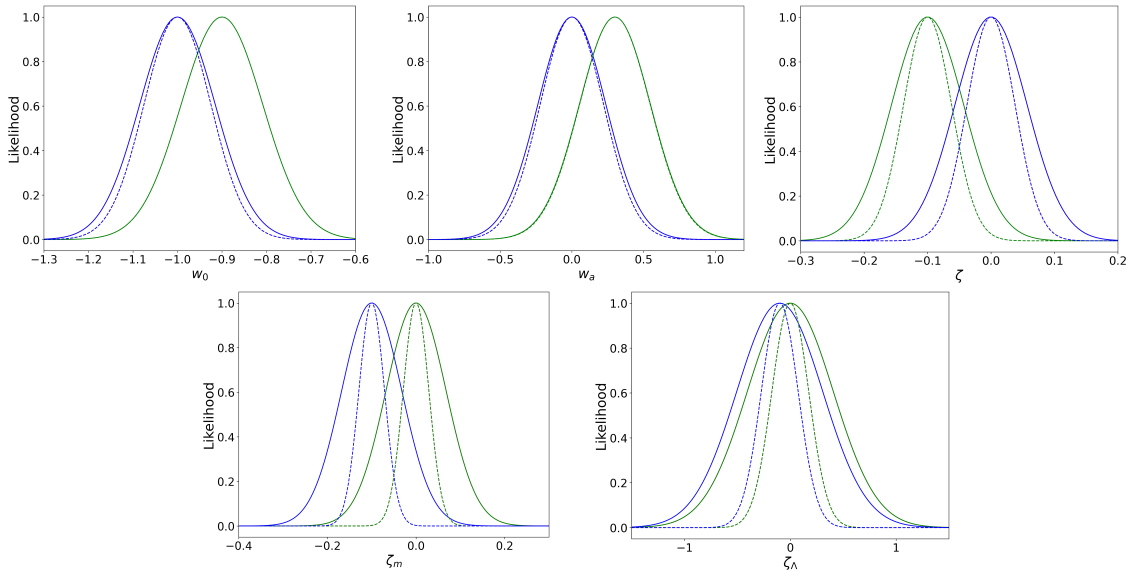

Figure 7.7: One-dimensional likelihoods for the w_0, w_a, ζ, ζ_m and ζ_Λ parameters for ΛCDM, Bekenstein and CPL models. The combinations of the Liske dataset with baseline and optimistic forecasts are the solid and dashed lines, respectively. Concerning the models, ΛCDM, CPL parametrization and Bekenstein correspond to the red, green and blue lines, respectively. The red lines drawn in the upper and bottom panels are not visible, as they are superimposed on the blue lines for w_0, w_a and ζ parameters and on the green lines for ζ_m and ζ_Λ parameters.

CHAPTER

8 Conclusions and Outlook

This master's thesis covers two types of spectroscopy tests of fundamental physics, measurements of the redshift drift and the value of the fine-structure constant, and returns the scientific impact of these measurements for possible ANDES configurations. It also identifies the key parameters for the respective scientific trade-offs.

The redshift drift and fine-structure constant value measurements were analyzed separately as well as in combination. And the gains of this combination were identified. The separate redshift drift analysis also includes the comparison of the approach used (Liske dataset) with the Golden Sample dataset and concluded that in the models studied the Golden Sample leads to weaker cosmological constraints. For the forecasts made for the measurements of the fine-structure constant value, as expected, an optimistic version, in general, allows us to obtain better parameter constraints.

As an output of this thesis, a scientific publication is being prepared that summarizes all the work developed in this thesis. The results obtained were also submitted to the scientific committee of two conferences, the conference Investigação Jovem da U.Porto (IJUP) and the 2022 edition of the Iberian Cosmology Meeting (IberiCOS 2022). Both abstracts have been accepted as oral communications, and were presented remotely (via Zoom) on May 4th.

During this dissertation and as part of one of the ESPRESSO Guaranteed Time Observations (GTO) scientific teams, I contributed to a paper that is already under revision.

For future research we suggest detailed analysis of the constraining power as a function of the number and precision of measurements and also the use of local experiments priors such as atomic clocks or Weak Equivalence Principle. In addition, updating the Golden Sample catalog may bring better results and therefore the need for its analysis. With ANDES already near the beginning of Phase B and ESPRESSO having started the GTO period, an application for a research fellowship in a PhD program has been submitted in order to continue the study of this master thesis.

Bibliography

[1] R. Caldwell. "A phantom menace? Cosmological consequences of a dark energy component with super-negative equation of state". In: *Physics Letters B* 545.1 (2002), pp. 23–29. ISSN: 0370-2693. DOI: https://doi.org/10.1016/S0370-2693(02)02589-3. URL: https://www.sciencedirect.com/science/article/pii/S0370269302025893 (cit. on p. xx).

[2] A. Friedmann. "Über die Krümmung des Raumes". In: *Zeitschrift fur Physik* 10 (Jan. 1922), pp. 377–386. DOI: 10.1007/BF01332580 (cit. on p. 3).

[3] G. Lemaître. "Un Univers homogène de masse constante et de rayon croissant rendant compte de la vitesse radiale des nébuleuses extra-galactiques". In: *Annales de la Société Scientifique de Bruxelles* 47 (Jan. 1927), pp. 49–59 (cit. on p. 3).

[4] E. Hubble. "A relation between distance and radial velocity among extra-galactic nebulae". In: *Proceedings of the National Academy of Sciences* 15.3 (1929), pp. 168–173. ISSN: 0027-8424. DOI: 10.1073/pnas.15.3.168. eprint: https://www.pnas.org/content/15/3/168.full.pdf. URL: https://www.pnas.org/content/15/3/168 (cit. on p. 3).

[5] C. Martins et al. "Real-time cosmography with redshift derivatives". In: *Phys. Rev. D* 94 (4 Aug. 2016), p. 043001. DOI: 10.1103/PhysRevD.94.043001. URL: https://link.aps.org/doi/10.1103/PhysRevD.94.043001 (cit. on p. 4).

[6] M. Murphy. "Electromagnetism: does its strength vary across the Universe?" In: *Australian Physics* 49 (2012), pp. 43–48 (cit. on p. 6).

[7] J. Uzan. "Varying Constants, Gravitation and Cosmology". In: *Living Reviews in Relativity* 14 (Sept. 2010). DOI: 10.12942/lrr-2011-2 (cit. on p. 6).

[8] J. Liske et al. "Cosmic dynamics in the era of Extremely Large Telescopes". In: *Monthly Notices of the Royal Astronomical Society* 386.3 (Apr. 2008), pp. 1192–1218. ISSN: 0035-8711. DOI: 10.1111/j.1365-2966.2008.13090.x. eprint: https://academic.oup.

com/mnras/article-pdf/386/3/1192/3611926/mnras0386-1192.pdf. URL: https://doi.org/10.1111/j.1365-2966.2008.13090.x (cit. on pp. 7, 19, 27).

[9] M. Martinelli et al. "Probing dark energy with redshift drift". In: *Phys. Rev. D* 86 (12 Dec. 2012), p. 123001. DOI: 10.1103/PhysRevD.86.123001. URL: https://link.aps.org/doi/10.1103/PhysRevD.86.123001 (cit. on p. 7).

[10] S. Lange and L. Page. "Detecting the Expansion of the Universe through Changes in the CMB Photosphere". In: *The Astrophysical Journal* 671.2 (Dec. 2007), pp. 1075–1078. DOI: 10.1086/523097. URL: https://doi.org/10.1086/523097 (cit. on p. 7).

[11] C. Alves et al. "Forecasts of redshift drift constraints on cosmological parameters". In: (July 2019). DOI: 10.1093/mnras/stz1934. URL: http://dx.doi.org/10.1093/mnras/stz1934 (cit. on pp. 8, 24, 29).

[12] P. Peebles and B. Ratra. "The cosmological constant and dark energy". In: *Rev. Mod. Phys.* 75 (2 Apr. 2003), pp. 559–606. DOI: 10.1103/RevModPhys.75.559. URL: https://link.aps.org/doi/10.1103/RevModPhys.75.559 (cit. on p. 8).

[13] P. Vielzeuf and C. Martins. "Varying constants and dark energy with the E-ELT". In: *Mem. Soc. Ast. It.* 85.1 (2014), pp. 155–160. arXiv: 1309.7771 [astro-ph.CO] (cit. on p. 9).

[14] M. Chevallier and D. Polarski. "Accelerating Universes with scaling Dark Matter". In: *International Journal of Modern Physics D* 10.02 (2001), pp. 213–223. DOI: 10.1142/S0218271801000822. eprint: https://doi.org/10.1142/S0218271801000822. URL: https://doi.org/10.1142/S0218271801000822 (cit. on pp. 9, 29, 35).

[15] E. Linder. "Exploring the Expansion History of the Universe". In: *Phys. Rev. Lett.* 90 (9 Mar. 2003), p. 091301. DOI: 10.1103/PhysRevLett.90.091301. URL: https://link.aps.org/doi/10.1103/PhysRevLett.90.091301 (cit. on pp. 9, 29, 35).

[16] H. Sandvik et al. "A Simple Cosmology with a Varying Fine Structure Constant". In: *Phys. Rev. Lett.* 88 (3 Jan. 2002), p. 031302. DOI: 10.1103/PhysRevLett.88.031302. URL: https://link.aps.org/doi/10.1103/PhysRevLett.88.031302 (cit. on pp. 10, 36).

[17] S. Howell. *Handbook of CCD astronomy*. Cambridge University Press, 2006, p. 208. ISBN: 9780521852159 (cit. on p. 14).

[18] P. Figueira, G. L. Curto, and A. Mehner. *Very Large Telescope Paranal Science Operations ESPRESSO User Manual*. European Southern Observatory. Garching bei München, 2021 (cit. on pp. 15, 17).

[19] L. Pasquini et al. "CODEX: An Ultra-stable High Resolution Spectrograph for the E-ELT". In: *The Messenger* (June 2010), p. 20 (cit. on p. 18).

[20] L. Origlia et al. "SIMPLE: a high-resolution near-infrared spectrometer for the E-ELT". In: *Ground-based and Airborne Instrumentation for Astronomy III*. Ed. by I. S. McLean, S. K. Ramsay, and H. Takami. Vol. 7735. International Society for Optics and Photonics. SPIE, 2010, pp. 912–920. DOI: 10.1117/12.856417. URL: https://doi.org/10.1117/12.856417 (cit. on p. 18).

[21] A. Marconi et al. "HIRES, the High-resolution Spectrograph for the ELT". In: *The Messenger* (Mar. 2021), pp. 27–32. URL: https://doi.org/10.18727/0722-6691/5219 (cit. on pp. 18, 27).

[22] M. Wilczynska et al. "Four direct measurements of the fine-structure constant 13 billion years ago". In: *Science Advances* 6.17 (Apr. 2020), eaay9672. DOI: 10.1126/sciadv.aay9672x. eprint: https://www.science.org/doi/pdf/10.1126/sciadv.aay9672. URL: https://www.science.org/doi/abs/10.1126/sciadv.aay9672 (cit. on p. 19).

[23] F. Aharonian et al. *Pathway to the Square Kilometre Array - The German White Paper* -. 2013. arXiv: 1301.4124 [astro-ph.IM] (cit. on p. 19).

[24] R. Carswell and J. Webb. *VPFIT: Voigt profile fitting program*. Aug. 2014. ascl: 1408.015 (cit. on p. 22).

[25] M. Murphy et al. "Further evidence for a variable fine-structure constant from Keck/HIRES QSO absorption spectra". In: *Monthly Notices of the Royal Astronomical Society* 345.2 (Oct. 2003), pp. 609–638. ISSN: 1365-2966. DOI: 10.1046/j.1365-8711.2003.06970.x. URL: http://dx.doi.org/10.1046/j.1365-8711.2003.06970.x (cit. on p. 22).

[26] J. King et al. "Spatial variation in the fine-structure constant - new results from VLT/UVES". In: *Monthly Notices of the Royal Astronomical Society* 422.4 (Apr. 2012), pp. 3370–3414. ISSN: 0035-8711. DOI: 10.1111/j.1365-2966.2012.20852.x. URL: http://dx.doi.org/10.1111/j.1365-2966.2012.20852.x (cit. on p. 22).

[27] J. Poyatos. "Testing the universality of physical laws: from ESPRESSO to the ELT". MA thesis. Polytech Clermont-Ferrand, 2021 (cit. on pp. 22, 23).

[28] V. Dumont. *QScan: Quasar spectra scanning tool*. Version v1.0.0. Mar. 2017. DOI: 10.5281/zenodo.597138. URL: https://doi.org/10.5281/zenodo.437903 (cit. on p. 23).

[29] M. Murphy et al. "Fundamental physics with ESPRESSO: Precise limit on variations in the fine-structure constant towards the bright quasar HE 0515-4414". In: *Astronomy & Astrophysics* 658 (Feb. 2022), A123. DOI: 10.1051/0004-6361/202142257. URL: https://doi.org/10.1051%2F0004-6361%2F202142257 (cit. on p. 23).

[30] A. Albrecht et al. *Report of the Dark Energy Task Force*. 2006. arXiv: 0609591 [astro-ph.IM] (cit. on p. 24).

[31] A. Albrecht et al. *Findings of the Joint Dark Energy Mission Figure of Merit Science Working Group*. 2009. arXiv: 0901.0721 [astro-ph] (cit. on p. 24).

[32] C. S. Alves et al. "Fisher matrix forecasts for astrophysical tests of the stability of the fine-structure constant". In: *Physics Letters B* 770 (July 2017), pp. 93–100. ISSN: 0370-2693. DOI: 10.1016/j.physletb.2017.03.053. URL: http://dx.doi.org/10.1016/j.physletb.2017.03.053 (cit. on p. 24).

[33] J. Darling. "Toward a direct measurement of the cosmic acceleration". In: *The Astrophysical Journal* 761.2 (Dec. 2012), p. L26. DOI: 10.1088/2041-8205/761/2/l26. URL: https://doi.org/10.1088/2041-8205/761/2/l26 (cit. on p. 27).

[34] R. Cooke. "The ACCELERATION programme: I. Cosmology with the redshift drift". In: *Monthly Notices of the Royal Astronomical Society* 492.2 (Dec. 2019), pp. 2044–2057. ISSN: 1365-2966. DOI: 10.1093/mnras/stz3465. URL: http://dx.doi.org/10.1093/mnras/stz3465 (cit. on p. 27).

[35] K. Boutsia et al. "The Spectroscopic Follow-up of the QUBRICS Bright Quasar Survey". In: *The Astrophysical Journal Supplement Series* 250.2 (Sept. 2020), p. 26. ISSN: 1538-4365. DOI: 10.3847/1538-4365/abafc1. URL: http://dx.doi.org/10.3847/1538-4365/abafc1 (cit. on p. 28).

[36] G. Calderone et al. "Finding the Brightest Cosmic Beacons in the Southern Hemisphere". In: *The Astrophysical Journal* 887 (Dec. 2019), p. 268. DOI: 10.3847/1538-4357/ab510a (cit. on p. 28).

[37] T. W. Anderson. *An introduction to multivariate statistical analysis*. Wiley New York, 1962 (cit. on p. 28).

[38] C. Wolf et al. "SkyMapper Southern Survey: First Data Release (DR1)". In: *Publications of the Astronomical Society of Australia* 35 (Jan. 2018). DOI: 10.1017/pasa.2018.5 (cit. on p. 28).

[39] Gaia Collaboration and A. Brown et al. "Gaia Data Release 2. Summary of the contents and survey properties". In: *Astronomy & Astrophysics* 616 (Aug. 2018), A1. DOI: 10.1051/0004-6361/201833051. arXiv: 1804.09365 [astro-ph.GA] (cit. on p. 28).

[40] H. Klöckner et al. "Real time cosmology - A direct measure of the expansion rate of the Universe with the SKA". In: May 2015, p. 027. DOI: 10.22323/1.215.0027 (cit. on p. 29).

[41] N. Aghanim et al. "Planck 2018 results: VI. Cosmological parameters". In: *Astronomy & Astrophysics* 641 (Sept. 2020), A6. ISSN: 1432-0746. DOI: 10.1051/0004-6361/201833910. URL: http://dx.doi.org/10.1051/0004-6361/201833910 (cit. on pp. 29, 31).

[42] C. Martins. "The status of varying constants: a review of the physics, searches and implications". In: *Reports on Progress in Physics* 80.12 (Nov. 2017), p. 126902. ISSN: 1361-6633. DOI: 10.1088/1361-6633/aa860e. URL: http://dx.doi.org/10.1088/1361-6633/aa860e (cit. on p. 35).

[43] C. Martins and A. Pinho. "Fine-structure constant constraints on dark energy". In: *Physical Review D* 91.10 (May 2015). ISSN: 1550-2368. DOI: 10.1103/physrevd.91.103501. URL: http://dx.doi.org/10.1103/PhysRevD.91.103501 (cit. on p. 35).

[44] C. Martins et al. "Fine-structure constant constraints on dark energy. II. Extending the parameter space". In: *Physical Review D* 93.2 (Jan. 2016). ISSN: 2470-0029. DOI: 10.1103/physrevd.93.023506. URL: http://dx.doi.org/10.1103/PhysRevD.93.023506 (cit. on p. 35).

[45] C. Martins et al. “Dark energy and equivalence principle constraints from astrophysical tests of the stability of the fine-structure constant”. In: *Journal of Cosmology and Astroparticle Physics* 2015.08 (Aug. 2015), pp. 047–047. ISSN: 1475-7516. DOI: 10.1088/1475-7516/2015/08/047. URL: http://dx.doi.org/10.1088/1475-7516/2015/08/047 (cit. on p. 35).

[46] C. Alves et al. “Current and future constraints on extended Bekenstein-type models for a varying fine-structure constant”. In: *Phys. Rev. D* 97 (2 Jan. 2018), p. 023522. DOI: 10.1103/PhysRevD.97.023522. URL: https://link.aps.org/doi/10.1103/PhysRevD.97.023522 (cit. on p. 36).

[47] T. Rosenband et al. “Frequency Ratio of Al+ and Hg+ Single-Ion Optical Clocks; Metrology at the 17th Decimal Place”. In: *Science (New York, N.Y.)* 319 (Apr. 2008), pp. 1808–12. DOI: 10.1126/science.1154622 (cit. on p. 36).

[48] E. Calabrese et al. “Dark Energy coupling with electromagnetism as seen from future low-medium redshift probes”. In: *Physical Review D* 89 (Nov. 2013). DOI: 10.1103/PhysRevD.89.083509 (cit. on p. 38).

ANNEX

I Annex 1

All the code produced for this dissertation can be found at: `https://drive.google.com/drive/folders/1YQpuy4lHJkkP8weprIppl-Je7YQGHS17?usp=sharing`. After the release of the scientific publication that summarizes all the work developed in this dissertation, this code will become public.